Optoelectronic Characterization of Photovoltaic Devices & Application of Nanofibers for Charge Storage

A thesis is submitted towards partial fulfillment of
BS-MS Dual Degree Program

By

Gadekar Akash Ramesh

Under the guidance of

Prof. Satishchandra B. Ogale

Chief Scientist Coordinator,

Center of Excellence in Solar Energy,

National Chemical Laboratory

INDIAN INSTITUTE OF SCIENCE EDUCATION AND RESEARCH
PUNE

Certificate

This is to certify that this thesis entitled **Optoelectronic Characterization of Photovoltaic Devices & Application of Nanofibers in Charge Storage** submitted towards the partial fulfillment of the BS-MS dual degree program at the Indian Institute of Science Education and Research Pune represents original research carried out by **Gadekar Akash Ramesh** at **National Chemical Laboratory**, under the supervision of **Prof. Satishchandra B. Ogale** during the academic year 2013-2014.

Mr. Gadekar Akash Ramesh	Prof. Satishchandra B. Ogale
Student Name	Supervisor Name

Acknowledgement

I would like to thank **Prof. Satishchandra Ogale**, my supervisor, for giving me an opportunity to work in his research laboratory. It was a truly great experience to work under his able guidance. I was very impressed by his attitude towards a particular problem. The way he enjoys science is marvelous. His dynamic personality inspired me immensely during this period. He not only helped develop my scientific temperament but also grafted me into a better human being.

I am really grateful to **Dr. Shouvik Datta**, my TAC (Thesis Advisory Comity) member. His expertise in the field of material science was really helpful to me.

I sincerely thank Indian Institute of Science Education and Research (IISER), Pune for providing the infrastructure and the high tech research labs, which contributed towards my scientific development. I thank National Chemical Laboratory (NCL) Pune, for allowing me to work there for a year. My special thanks to Kishor Vaigyanic Protsahan Yojana (KVPY), Bangalore for funding my work.

I would also like to thank **Mr. Onkar Game**, and **Mr. Raunak Naphade** for their mentoring and encouragement during my research days. I would like to thank all my colleagues and lab mates for providing a very friendly environment in the lab. Finally, I would like to thank my parents and my sister, for their love and care. Last but not the least; I thank Lord Ganesha for always being with me.

Akash Gadekar

Abstract

The Dye Sensitized Solar Cells (DSSCs) have shown very less improvement in photo-conversion efficiency in the last decade. The basic understanding of these devices is still not very sound. The oxygen vacancies in TiO_2 substrate have a significant role in the performance of DSSC. The optoelectronic transient technique is one of the crucial measurements employed to study the fundamental properties of DSSC's.

In this work we have used optoelectronic current and voltage transient measurements and electrochemical impedance spectroscopy as tools to study the performance of DSSC's with respect to the presence of oxygen vacancies. The brief introduction to the thesis is presented in **chapter 1**. A brief overview of the characterization techniques of the photovoltaic devices is presented in **chapter 2** along with a general outline of the instruments and methods used for the characterization of the nanomaterials. **Chapter 3** comprises of the detailed analysis on the effect of oxygen vacancies on the performance of dye sensitized solar cells.

Recently, nanofibers have got a very high significance due to their interesting opto-electronic properties over other nanostructures. Hence we synthesized nanofibers with a self-designed electro-spinning instrument and used these for different energy applications. In section B**, chapter 4** is dedicated to the general introduction of 1D nanostructures of metal oxides and carbon based nanostructures and their characterization tools.

The application of Au-TiO_2 nanostuctures as a scattering layer in quantum dot solar cells is discussed in **chapter 5**. $NiFe_2O_4$ – CNF (carbon nanofibers) as a cathode material for hybrid supercapacitor is discussed in **chapter 6.**

Contents:

Section A

Chapter 1: Introduction to Dye Solar Cells

1.1 Energy Sources

Energy is one of the most important needs of human life. Currently over 80% of the energy needs are satisfied through conventional fossil fuels, such as natural oils, natural gas, and coal. However, the resources of these fossil fuels are limited. If this trend continues the world would be out of energy in the next 100 years. To satisfy the energy requirements, we need to develop and start using renewable sources of energy. Today renewable energy is mostly dependent on Biomass energy which covers about 74% of the renewable energy spectrum. The clean renewable energy sources such as hydrothermal elecricity, solar energy, wind energy, etc. contibute to only 4% of the overall energy consumption.

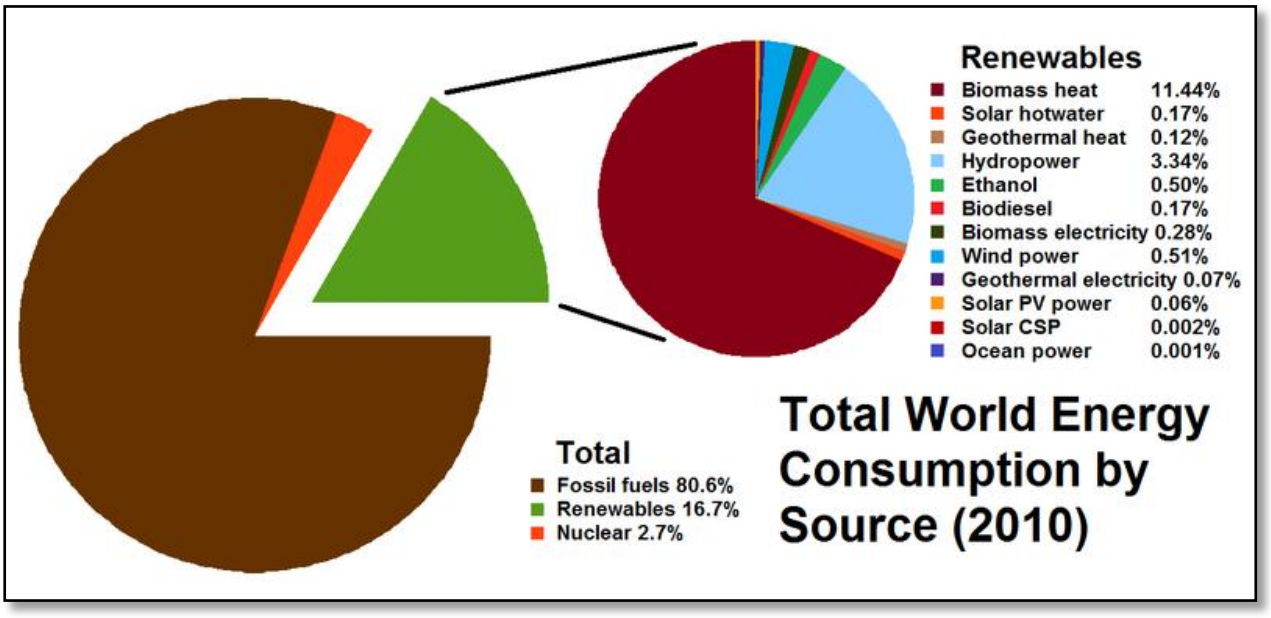

Figure 1.1: Total world energy consumption by source 2010, from REN21 Renewables 2012 Global Status Report

Biomass energy is the energy generated from plants and animals. It can either be directly used by burning wood or animal wastes, or can be converted into biofuels such as methane. However, the problem with this energy is that it is not

environment friendly. It produces carbon dioxide, which is unacceptable. The hydroelectric power is generated from water stored in dams, which drives the water turbines and generators. This mechanical energy is converted into electric power. Wind power utilizes the energy of blowing wind, which rotates the blades of windmills and generates electricity. The hot rocks present under the ground heat water, and the subsequent steam produced drives the turbines. This is how geothermal energy is converted into electricity.

Unlike solar energy other renewable energy resources have limitations in their usage. After a certain point in time, the energy output from these resources would hardly increase. They cannot be used at all geographical locations throughout the year. However, solar energy is available almost everywhere throughout the year. Sunlight which reaches earth mainly consists of infrared, visible and ultraviolet light. The current energy need of all human beings is around 10TW. We could use all the available energy from renewable energy resources: hydroelectric power (0.5TW), tides and ocean currents (2TW), geothermal energy (12TW), globally extractable wind power (3TW) and solar energy received by earth (120,000TW) to sustain our energy requirements. Amongst all these choices, solar energy is the most feasible source for our future energy demands. Solar energy is used conventionally by plants to produce carbohydrates from carbon dioxide and water in the presence of sunlight, a process called photosynthesis. Other than photosynthesis, solar energy is hardly utilized for any other energy requirement. Solar thermal energy is used in certain developing countries to heat water and to cook food. However, the commercial production of electricity from solar photovoltaic has not yet been exploited in a humongous manner.

However, many initiatives have been undertaken recently for the use of solar power. They are:

1. Concentrated Solar Power (CSP): These systems use lens, mirrors, and tracking systems to focus a large area of sunlight into a small beam, which is then used as a heat source for conventional power plants.
2. Concentrated Solar Thermal Power: In these cells, solar thermal energy is converted into electrical energy.
3. Photovoltaic Power: Photovoltaic cell converts photon energy into electrical energy using photovoltaic effect.

1.2 Photovoltaic Cells:

Photovoltaic cells can be classified broadly under three generations according to their evolution. The majority of solar cells used today are first generation solar cells based on crystalline silicon. Silicon based solar cells contribute to 90% of the total production of cells in the market today. The production cost presently is $3/Wp. The second generation solar cells, called thin film solar cells, include cadmium telluride (CdTe), copper indium gallium selenides (CIGS), amorphous Si, etc. The theoretical photon to electrical current conversion efficiency of a single crystalline solar cell is about 33%; the practically achieved value is up to 26%. The problem with silicon based solar cells is the cost of production of crystalline silicon wafer and with second generation solar cells is the use of toxic materials such as Cd, Se, etc.

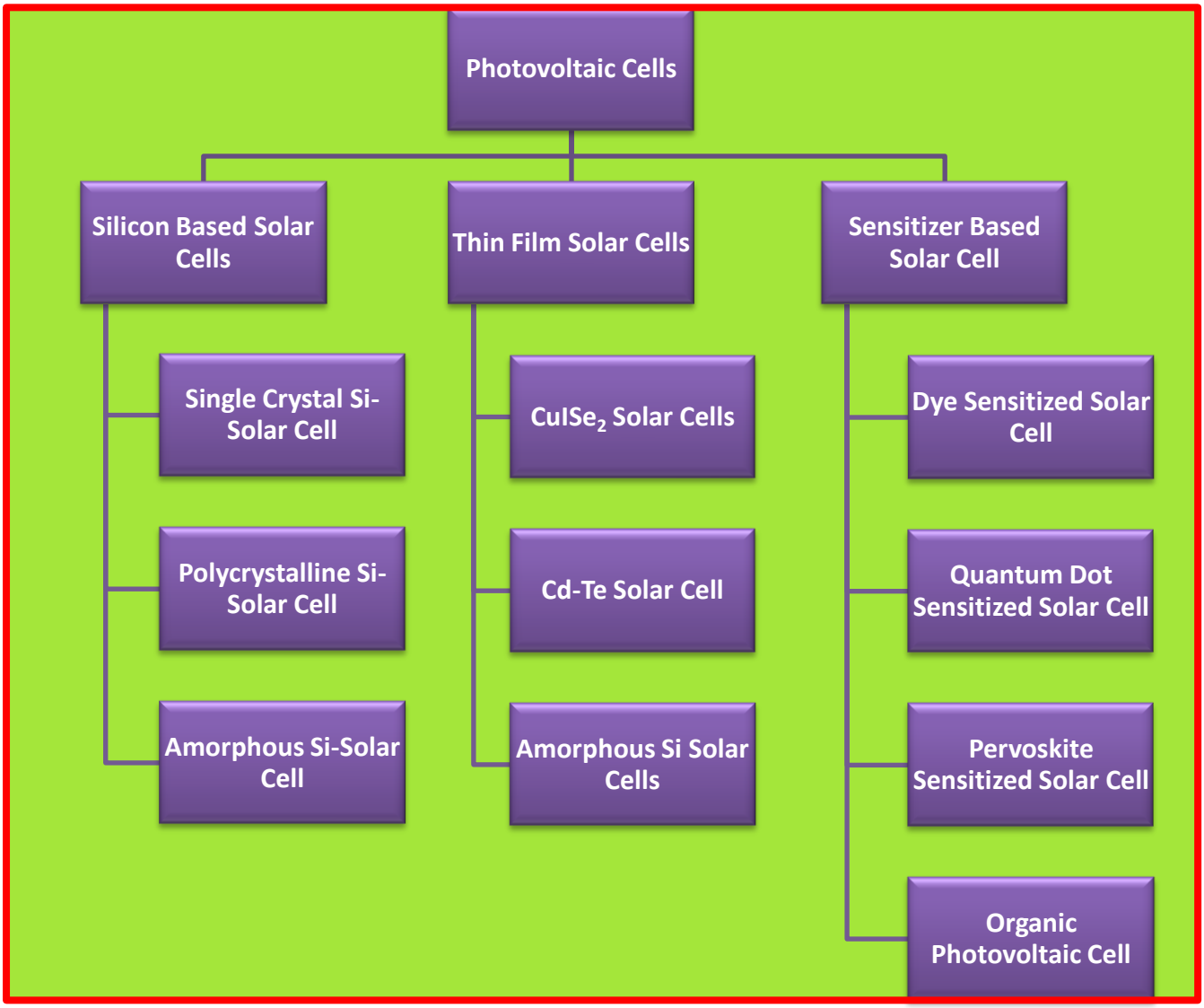

Figure 1.2: Hierarchy of Phototvoltaics Cells

In 1990, a new concept of solar cells was conceived. These are the third generation of photovoltaics. [1] Unlike the traditional p-n hetero-junction solar cells, these are sensitizer based photovoltaic cells. The idea for these photovoltaics came from the natural light harvesting phenomenon of photosynthesis. Many categories of solar cells come under this generation depending upon the type of sensitizer used, those are:

1. Dye Sensitized Solar Cells (DSSC)
2. Quantum Dot Sensitized Solar Cells (QDSC)
3. Pervoskite Sensitized Solar cells
4. Organic bulk heterojunction photovoltaic cells

These cells have overcome the Shockley-Queisser limit of maximum conversion efficiency. [2] The other two are more recent categories of cells, pervoskite based solar cells were invented in the year 2013. These third generation solar cells are based on nanotechnology. There are so many parameters to play with; hence it is very difficult to achieve very high efficiency using these cells. The highest efficiency achieved by dye sensitized solar cells till today is 12%. [3]

A study in 2003 concluded that the world could generate 2,357,840 TWh each year from very large scale solar power plants using 1% of each of the world's deserts. Total consumption worldwide was 15,223 TWh/year[42] (in 2003).

1.3 Dye Sensitized Solar Cells (DSSC):

1.3.1 Structure of DSSC:

For preparation of DSSC, we followed the standard procedure developed and optimized by Michael Grätzel, et.al. [4] The DSSC consists of 5 main components such as follows:

1. Substrate: These are highly transparent glasses. They are coated with conducting metal oxides. The transparent conducting oxide (TCO) generally used is either fluorine doped tin oxide (FTO) or indium doped tin oxide (ITO). The TCO should have low sheet resistance (10-15 Ω per square). It provides the mechanical integrity to the solar cell and protects it from the environment.

2. Metal Oxide Layer (Anode material): Metal oxide coating is deposited over TCO by doctor blading or screen printing method. [5] In these solar cells, ZnO and TiO_2 are preferable metal oxides. This layer is around 10µm. It is a mesoporous network of metal oxide nanoparticles. The dye molecules are adsorbed on the surface of this layer. Higher the surface area more would be the dye adsorption. Experimentally it was observed that the anatase form of TiO_2 is the best metal oxide material for DSSC.

3. Sensitizer (Dye): Sensitizer is the key component of DSSC. It absorbs the sunlight. The metal oxide films are immersed in the dye solution for 12 to 24 hours so that the dye molecules get adsorbed on the surface of the metal oxide nanoparticles. The dye we used is N719 dye {Di-tetrabutylammonium cis-bis(isothiocyanato)bis(2,2'-bipyridyl-4,4'-dicarboxylato)ruthenium(II)} red colored. The structure of this Ruthenium based organic dye is shown in figure1. [6]

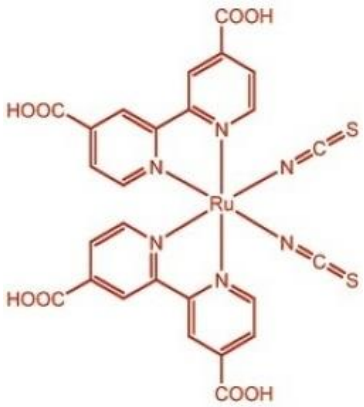

Figure 1.3: N719 Dye

4. Electrolyte: The electrolyte is a redox (reduction-oxidation) couple. Typically iodine/iodide redox couple is used. The iodine/iodide electrolyte is prepared simply by mixing iodine with an iodide salt in an appropriate solvent, like acetonitrile or methoxypropionitrile. The liquid electrolyte puts limitations on the applications of these devices. Hence for better performance these devices need to be perfectly sealed. For solid state devices OMeTAD is used. It acts as a sensitizer as well as a hole transporter.

5. Counter Electrode (Cathode): There are many types of counter electrodes. The most robust is the Platinum based counter electrode. A thin layer of Pt catalyst is prepared by simply drop casting Platisol ($PtCl_4$) on CTO and annealing it at 450^0C. As Pt is very costly, people are trying to synthesize sophisticated carbon based counter electrodes for DSSC.

1.3.2 Basic Principle of working of a Dye Sensitized Solar Cell:

Unlike the conventional solar cells, in which the minority carriers are drifted away from the space charge layer by the electric field, electrons and holes are diffused through the multilayered structure of DSSC. The DSSC is a bio-inspired photovoltaic device, which works on the principle of artificial photosynthesis. Similar to natural photosynthesis, in which the light photon is absorbed by the chlorophyll pigment present in the leaves, the sensitizers, which are natural dyes (S), absorb light photons. The electrons from HOMO are excited to the LUMO, and an exciton pair is generated. The maximum light wavelength absorbed by N719 dye is 540nm.

An electron is injected into the conduction band of the metal oxide (TiO_2). The electron diffuses through the polycrystalline mesh of TiO_2, and is liberated at the CTO (anode or working electrode). The sensitizer is regenerated by the electron transfer from the electrolyte. The reducing species from the electrolyte (I^-, iodied ion) gives an electron to the sensitizer and gets oxidized (I_2; iodine). The hole is carried away through the electrolyte by the I_3^- (triiodide) ions and delivered at the cathode (counter electrode).

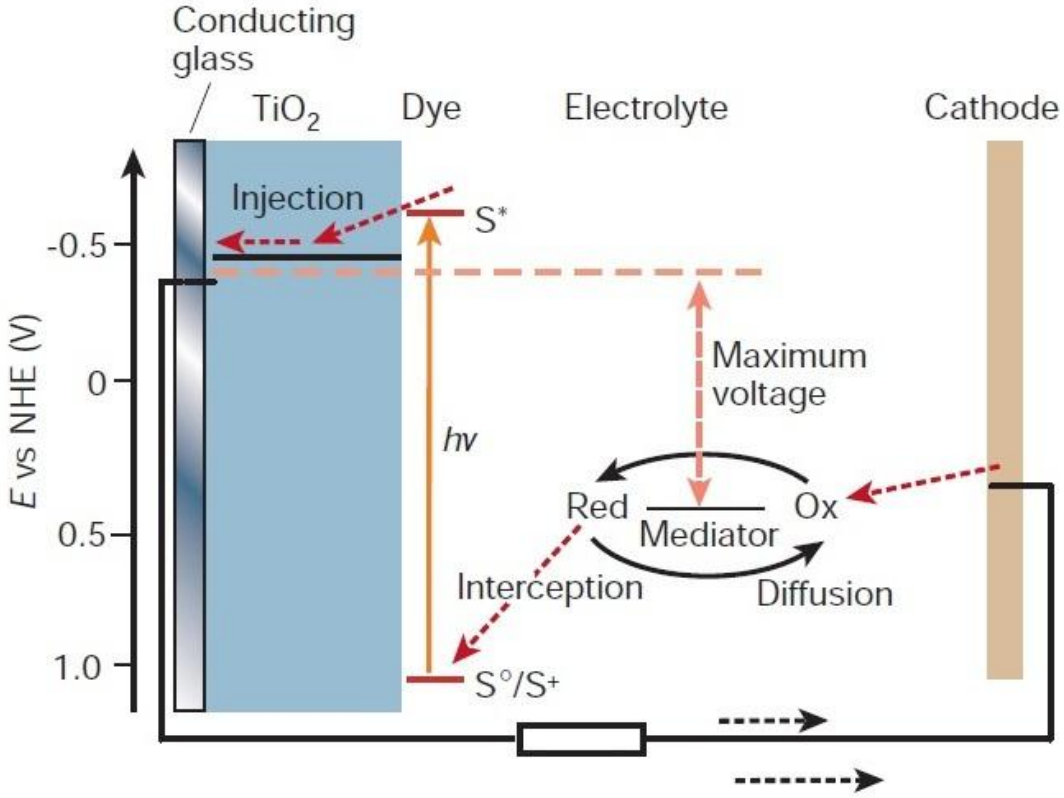

Figure 1.4: Working principle of DSSC

1.3.3 Electron transfer processes in DSSC:

DSSCs are photochemical devices in which several electron transfer processes are in competition with each other.

Reaction			Name	Lifetime
$S\|TiO_2 + hv$	→	$S^*\|TiO_2$	Photo-excitation	10^{-12}s
$S^*\|TiO_2$	→	$S^+\|TiO_2 + e_{cb}(TiO_2)$	Charge injection	10^{-15}s
$S^*\|TiO_2$	→	$S\|TiO_2$	Relaxation	10^{-9}s
$S^+\|TiO_2 + 3/2\ I^-$	→	$S\|TiO_2 + ½\ I_3^{-\bullet}$	Regeneration	10^{-6}s
$S^+\|TiO_2 + e^-(TiO_2)$	→	$S\|TiO_2$	Recombination	10^{-3}s
$e^-(TiO2) + ½\ I_3^-$	→	$3/2\ I^-$	Back reaction	10^{-3}s
$e^-(Pt) + ½\ I_3^-$	→	$3/2\ I^-$	Catalytic reaction at Pt	10^{-3}s

Table 1.1: Electron Transfer process in DSSC

As there are several back reactions, we need to check the lifetime scales of these reactions. Figure shows typical time constants of processes involved in such a DSSC device. Under illumination, the sensitizer is photo-excited in a timescale of femtoseconds and electron is injected ultrafast from S* to the conduction band of TiO_2 on picoseconds timescale. The nanosecond-ranged relaxation of S* is thousand times slower than injection, ensuring the injection efficiency to be unity. The ground state of the sensitizer is then recovered by I^- in the microsecond domain, effectively regenerating S and intercepting the recombination of conduction band electron in TiO_2 with S^+, which happens in the millisecond timescale. This is followed by percolation of electron across the nanocrystalline film and the redox capture of the electron by the oxidized relay (back reaction) I_3^-, within milliseconds or even seconds. The similarity in time constants of both the processes says that the recombination reaction plays a major role in hampering the high conversion efficiencies in DSSC.

2. Device Characterization Techniques:

2.1 IPCE (Incident Photon Conversion Efficiency):

It is a very fundamental method to check the performance of a solar cell device. It is also called as external quantum efficiency. It is the percentage of incident photons that are successfully converted into current under a monochromatic illumination. It is measured by using a monochromator, usually ranging from 200nm to 800nm.

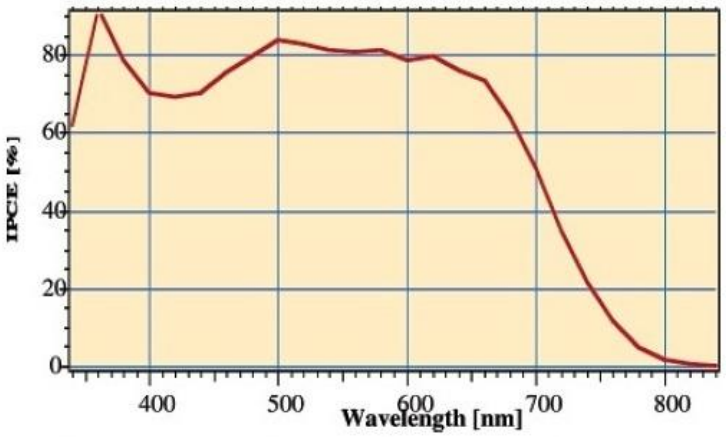

Figure 2.1: IPCE of N719 Dye

2.2 Current voltage characteristics:

This is a very useful technique used to calculate the efficiency of the device. It consists of parameters like Voc, Jsc, Fill Factor, and efficiency. Figure 2.2 shows the ideal characteristics of J-V curve.

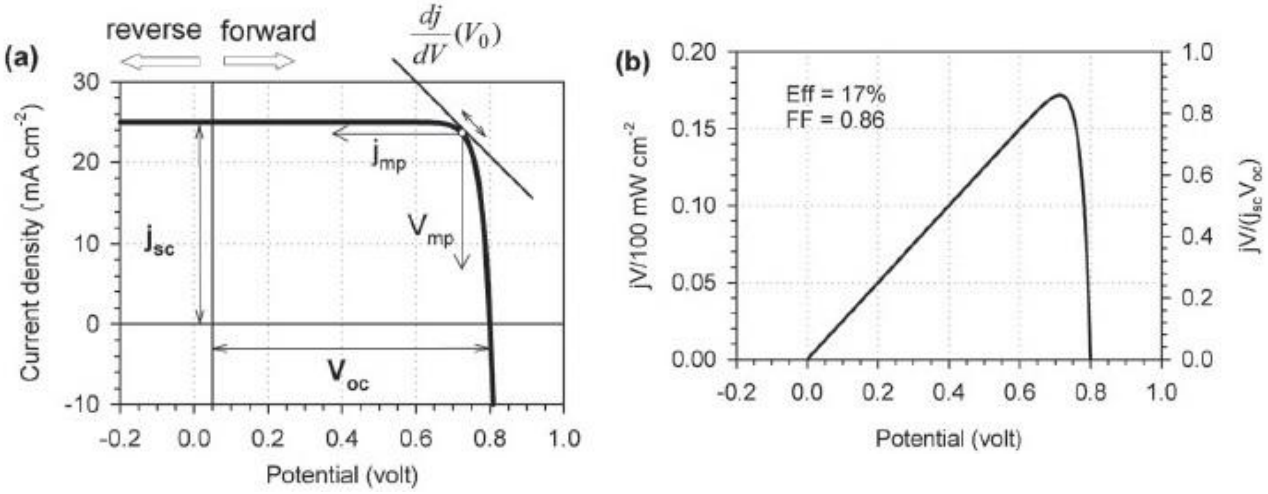

Figure 2.2: (a) Ideal J-V Curve of photovoltaic devices, (b) corresponding power extraction

a) Open circuit Voltage (V_{oc}): The photovoltage generated by the cell is the difference between the Fermi energy level in semiconductor under illumination and the Nernst potential of redox couple in the electrolyte. It is the maximal voltage produced by the cell. The excitation by light produces excess electrons and holes in the carrier bands, which causes the separation of the Fermi levels, of the two states in the absorber. We can define a Fermi level (or internal) voltage V_F as the difference of electrochemical potential of electrons (E_{Fn}) and holes (E_{Fp}) in the materials.

$$V_F = \frac{(E_{Fn} - E_{Fp})}{q}$$

b) Short circuit current density (J_{sc}): It is basically extraction of the photogenerated electrons and holes. It is the maximum current through the circuit, when the resistance is zero.

c) Filling Factor (FF): It is the measure of squareness of the I-V curve. It primarily depends on the series and shunt resistances. For ideal fill factor series resistance should be zero, while shunt resistance should be infinity. Series resistance and shunt resistance are inverse of a slope of I-V curve at open circuit and short circuit voltage respectively.

$$FF = \frac{I_m * V_m}{I_{sc} * V_{oc}}$$

where I_m and V_m are current and voltage corresponding to maximum power point.

d) Light to electric current conversion efficiency (η):

$$Efficiency\ (\eta) = \frac{\mathrm{V_{oc}} * \mathrm{J_{sc}}}{\mathrm{I_{in}}} * \mathrm{FF} * 100\ \%$$

I_{in} is the input power of the solar simulator. It is an important experimental parameter and in order to compare different results, standard test condition is always used for all the devices in this work. This condition includes AM 1.5 spectrum illumination with an incident power density of 100 mW cm^{-2} and a test temperature of 298 K.

2.3 Electrochemical Impedance Spectroscopy (EIS):

EIS technique was developed by Juan Bisquert, Francisco Fabregat-Santiago, et. al. for device characterization. It consists of the frequency analysis of ac behavior and is broadly applied in a broad class of material systems and devices. EIS has been applied generally to investigate transport and recombination properties of many different kinds of Solar Cells.[10–12] Measurement of EIS at each point allows us to separate resistances and capacitances by providing detailed information about the electronic process at that point. Separation of different components of the resistance using EIS, and their distinct analysis as a function of voltage, is a very effective tool to determine the properties of the solar cell. [9]

Procedures:

In this technique, the cell is set at a fixed reverse bias voltage. In this equilibrium condition a small voltage pulse is given.

$V = V_0 \sin(\omega t)$ where ω is a frequency

Due to the presence of resistances and capacitances in the device, corresponding current is

$I = I_0 \sin(\omega t + \varphi)$ where φ is the phase difference

Now the impedance of the system is given as

$Z = \frac{V}{I} = \frac{V_0 \sin(\omega t)}{I_0 \sin(\omega t + \varphi)} = Z_0 e^{i\varphi}$ where Z_0 is a magnitude of impedance.

The frequency range chosen for this measurement is from 10^{-2}Hz to 10^{6}Hz and the ac amplitude of the voltage pulse to be 10mV. Resistance in general describes electron transfer or transport events, whereas capacitances relate to electronic carrier accumulation and distribution in the device.

The typical Nyquist plot for DSSC looks as shown in the figure 2.3. It has generally 3 semicircles. They are attributed to Pt | Electrolyte (Z_1), TiO_2 | Dye | Electrolyte (Z_2) and diffusion of I_3^- (Z_3). This curve is fitted with appropriate equivalent circuit as shown in the figure 2.4. Typically for DSSC, equivalent circuit used is based on the transmission line model given by Bisquert et.al.[9, 21]

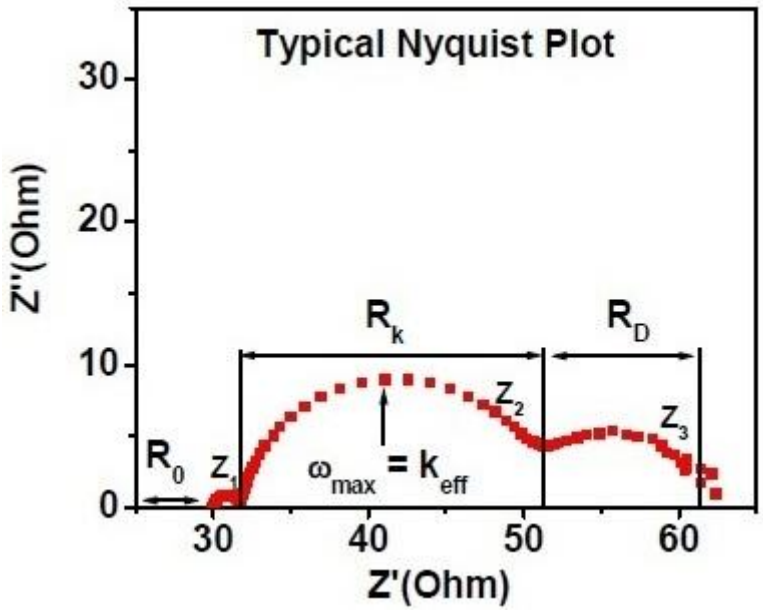

It starts with high frequency region to the low frequency region. R_k is the charge transfer resistance. R_D is the resistance to diffusion of holes in electrolyte.

Figure 2.3: Typical Nyquist Plot for Dye Sensitized Solar Cell

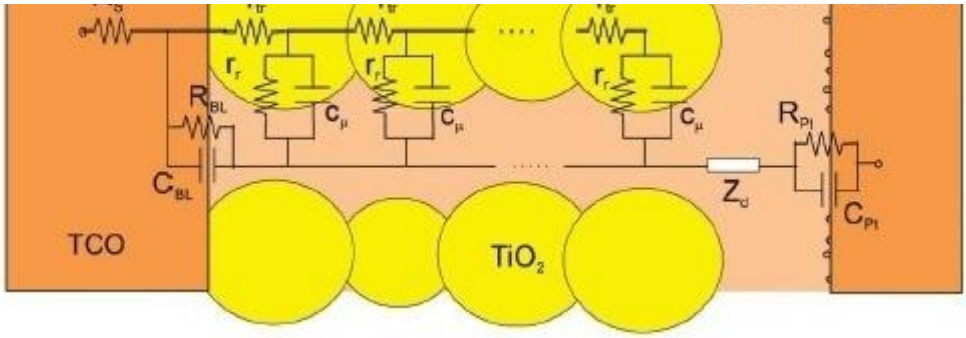

Figure 2.4: Transmission Line Model for DSSC

This model is useful in calculating the various parameters of solar cells, such as recombination resistance (r_r), transport resistance (r_{tr}), and chemical capacitance (Cμ). From these parameters one can explain trap state density, transport and recombination processes of solar cells.

2.4 Optoelectronic current and voltage transient spectroscopy:

The automated instrument for transient photocurrent and transient photovoltage measurement was designed by Brian Oregan and Piers Barns from

Imperial College London. The equipments are relatively cheap and faster than EIS. It requires a computer, data acquisition (DAQ) card, white and red LEDs with power supply and 2 transistor switches. The advantage of this type of transient system is that it can be used to study a variety of devices at wide range of operating conditions.

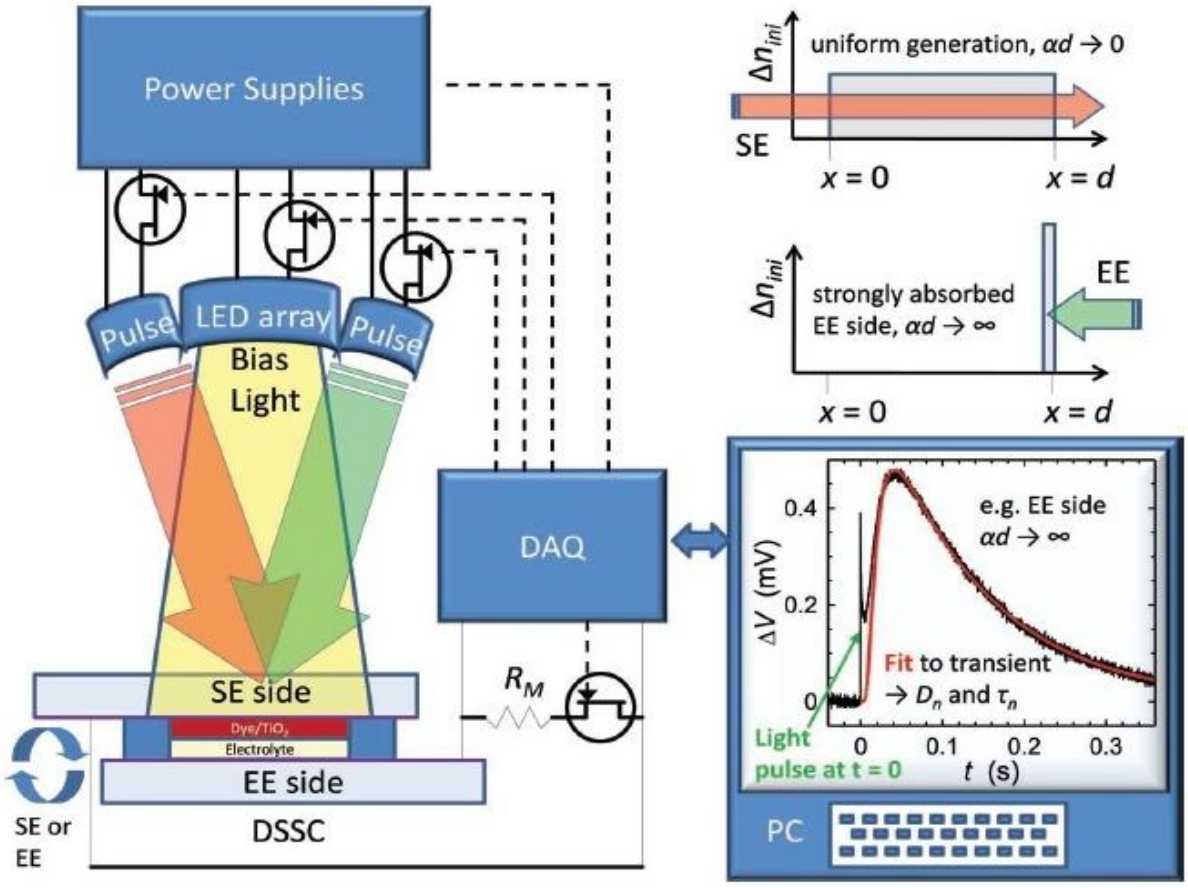

Figure 2.5: Transient Setup and the signals recorded

Information about electron concentration, transport, and recombination is extracted from this measurement. This model is based on exponential distribution of trapping states. [13] Charge extraction or capacitance measurements enable the size of this conduction band shift to be estimated by assuming that the distribution of trap states relative to the conduction band edge remains unchanged.

Transient Measurement Setup:

We followed a protocol made freely available by Brain O'Regan. 10 white Light Emitting Diodes (LEDs; 3W each) were used to generate background

illumination. By applying constant current source, illumination can be controlled from 0.01Sun to 2Sun (where 1Sun is typical brightness of Sun). 5 red light LEDs (1W each, $\lambda_{max} \approx 630nm$) were arranged in between the white LEDs, which were used to generate pump pulse. LEDs were controlled by fast solid-state MOSFET switch (response time <1 μs, capacitance <50 nF). In order to discern the small perturbation measurements the intensity and duration of the pump pulse was adjusted so that the perturbations were relatively small as compared to the background photovoltage or photocurrent and of shorter duration than the response time of the signal of interest. A National Instruments data acquisition card was used to record the time resolved voltage and current measurements. For photovoltage transient measurements (PVT) the cell was stabilized for 10 – 100 s under bias light so as to reach equilibrium operating conditions, the illumination pulse duration normally ranged between 10–100 μs, and the time required for signal acquisition ranged between 0.05–4s. The cell was stabilized under steady state bias light for 10–20s before measurement of a photocurrent transient. The illumination excitation pulse time ranged between 6–13 μs, and the signal acquisition time ranged between 0.025–10s, an average of 3–8 photocurrent transient signals were recorded. [20]

Charge Extraction

This method is used to record the quantity of charge stored within a cell under given operational conditions with a particularly applied voltage under dark or light conditions. [13] This involves integrating the total current extracted from the cell, and then immediately switching the light off and simultaneously setting the cell to short circuit using fast, solid state switches. [14] The initial steady-state starting condition from which the measurement is made can be any point on a j-V curve. [20]

Chapter 3: Oxygen Vacancy Problem

3.1 Introduction

Oxygen vacancies play a very important role in controlling optoelectronic properties of metal oxides used in DSSCs. Increased oxygen vacancy concentration within TiO_2 is shown to enhance its visible light photo-catalytic/photo-electrochemical activity. [15] However, there is no consensus in literature regarding the beneficial or detrimental role of oxygen vacancies (and other defect types) on the properties of DSSCs. Improvement in DSSC efficiency with Lanthanum or Boron [16, 17] doping has been attributed to increased oxygen vacancy concentration for charge balance. On the contrary, oxygen plasma treatment, [18] is used to decrease the oxygen vacancies on the surface of TiO_2 nanoparticles resulting in enhanced photo-conversion efficiency. Meng et. al. [19] have predicted through time dependant density functional theory that oxygen vacancy defects can result in better dye adsorption and facilitate the charge injection but at the cost of lower open circuit voltage and higher e-h recombination rate. In order to investigate the role of oxygen vacancies in TiO_2 we followed two approaches whose justification is given as follows

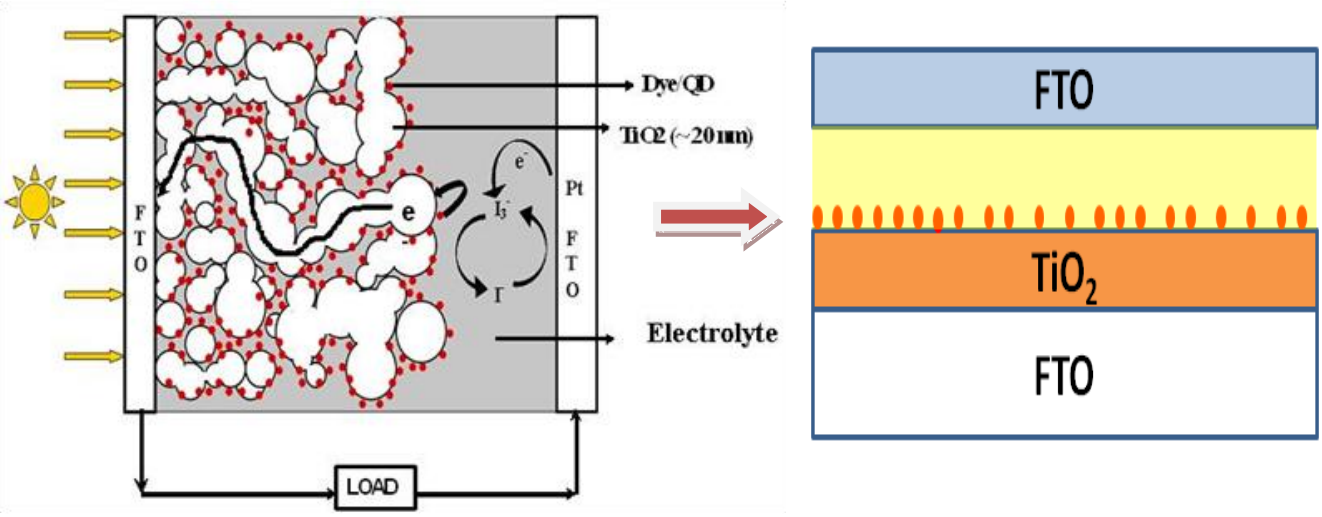

Figure 3.1: Complex Assembly of DSSC is simplified by preparing TiO_2 film using Pulse Laser Deposition (PLD)

1. **The thin film approach using Pulsed Laser Depostion (PLD) technique**:

Although much of the DSSC action occurs at these interfaces, they have remained ill-understood because, being embedded, they are hardly accessible to direct surface/interface probes. Herein we have employed a thin film platform (growth parameter controlled pulsed laser deposited TiO_2 films) to examine the TiO_2-Dye-Electrolyte system. Even though the very low surface area of pulsed laser deposited non-porous (dense) thin film (in comparison with the mesoporous DSSC architecture) results in very low dye adsorption, the solar cell parameters are still measurable and bring out some very interesting information.

2. **The mesoporous TiO_2 based working DSSC device approach**:

In this case we prepared the working DSSCs with mesoporous TiO_2 films deposited on FTO substrates. The reference sample was annealed in air whereas the oxygen deficient device was prepared by annealing the TiO_2 film in Vacuum. The results obtained with mesoporous DSSC approach were compared with the results in thin film approach. The meosoporous approach also helped to carry out transient optoelectronic measurements on oxygen deficient TiO_2 based DSSCs which yielded vital information regarding the band edge shift, electron-hole lifetime etc.

3.2 Experimental:

A) Device Fabrication:

a) Thin Film approach:

A KrF excimer laser (= 248 nm, 20 ns pulses, Rep rate 10 Hz, energy density = 2.5 J /cm^2) was used to ablate the TiO_2 target. Non-porous TiO_2 films (150 nm) were deposited on FTO target under different oxygen partial pressures viz. 10^{-5}, 10^{-3}, 10^{-1} mbar. Such films were immersed in 0.5mM ethanolic solutions of N719 dye for two hours to adsorb a monolayer of dye and then rinsed with absolute ethanol to remove the excess dye. DSSCs (0.25 cm^2) were then fabricated using a sandwich assembly of Pt coated FTO counter electrode and I^-/I_3^- electrolyte.

b) Mesoporous DSSC approach:

Fluorine doped tin oxide (FTO) substrates were cleaned by sonicating in detergent solution, deionised (DI) water, and ethanol, about 15 min each. The TiO_2 based paste was purchased from Dyesol. The paste was homogeneously spread on the FTO by doctor blading technique. This transparent nanocrystalline TiO_2 photoanode was calcined at 450^0C for 30 min to remove organic content. Thickness of this TiO_2 layer was kept around 13 µm. These films were treated with $TiCl_4$ (50mM) at 75^0C for 30 min. To create oxygen vacancies in the TiO_2 layer, this TiO_2 substrate was annealed in vacuum (10^{-5} mbar pressure) in a vacuum chamber at 450^0C for 3 hours. For comparison another TiO_2 substrate was annealed in Air (atmospheric pressure) at 450^0C for 3 hours. These electrodes were soaked in 0.5 mM N719 dye solution for 24 hours. Films were washed with ethanol to wash out un-adsorbed excess dye molecules. The counter Pt electrode (photocathode) was prepared by drop casting Platisol (H_2PtCl_6) (Solaronix) and annealed at 400^0C for about 15 min. These two electrodes were sealed using a sealant surlyne (Solaronix). Space between the two was filled by an electrolyte which consists of 0.1 M lithium iodide (LiI), 0.05 M iodine (I2), 0.6 M 1-hexyl-2,3-methylimidazolium iodide and 0.5 M 4-tertbutylpyridine in acetonitrile and valeronitrile (1 : 1 v/v).

3.3 Results and Discussion

3.3.1 Photovoltaic Characterization IV of Thin Film Devices prepared by PLD:

Thin TiO_2 films were pulsed laser deposited under different oxygen partial pressure (10^{-5}, 10^{-3}, 10^{-1} mbar) in order to vary the oxygen vacancy concentration within TiO_2 film. These films were sensitized with N719 dye in order to study their photovoltaic performance. Figure 3.2 shows (a) IV and (b) IPCE curve for pulse laser deposition (PLD) films. The table 3.1 shows J-V parameters of the PLD TiO_2 films deposited under different oxygen partial pressure.

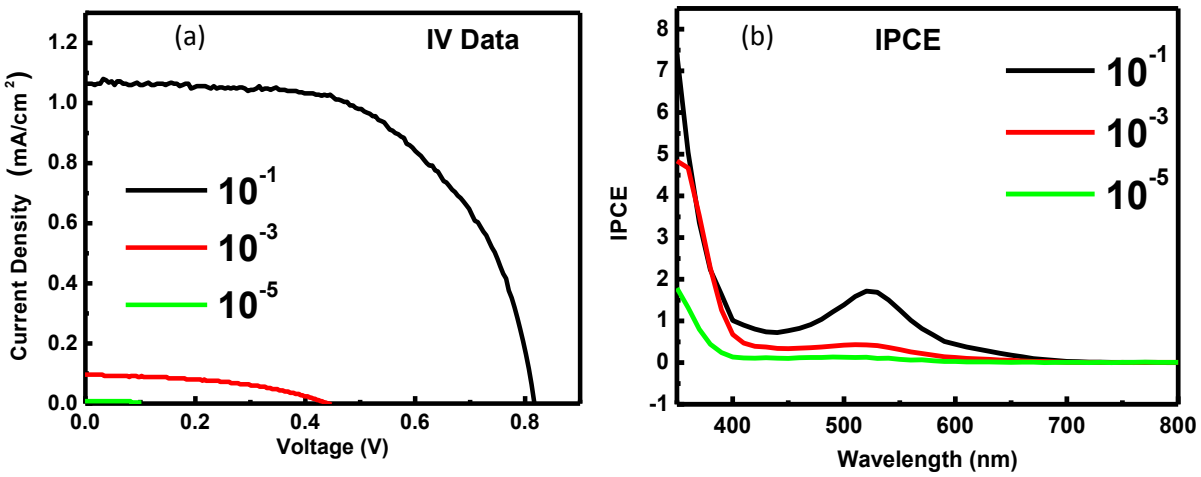

Figure 3.2: (a) J-V and (b) IPCE data of PLD sintered films.

Note that the lower value of efficiency is due to two reasons. Firstly the TiO_2 films are not porous hence have very small surface areas. Secondly only monolayer of dye is adsorbed on these films, which leads to very low photo-excitations hence the low value of efficiency.

Film (Pressure) Torr	V_{oc} (V)	J_{sc} (mA/cm^2)	FF	Efficiency
10^{-1}	0.81	1.06	58.3%	0.5%
10^{-3}	0.44	0.095	44.1%	0.018%
10^{-5}	0.17	0.0072	43.3%	0.0005%

Table 3.1: J-V parameters of the PLD sintered film

It can be seen that as the oxygen partial pressure within deposition chamber of PLD system decreases it leads to increased concentration of oxygen vacancies in TIO_2 resulting in lower photo-voltaic performance. In particular as the deposition pressure decreases from 10^{-1} mbar to 10^{-5} mbar the open circuit potential decreases from 0.81V to 0.17 V. The decreased value of open circuit potential points towards dramatically increased recombination rate in TiO_2 with oxygen vacancies. The increased recombination in case of oxygen deficient TiO_2 films also leads to decreased short circuit current. This is also confirmed from the Incident Photon to Current conversion Efficiency (IPCE). Clearly the TiO_2 film with high oxygen vacancies gave negligible IPCE in the region of absorption of dye (450nm to 650nm) resulting in less photocurrent.

3.3.2 Mesoporous TiO_2 DSSC optoelectronic Characterization:

J-V curves:

In order to correlate the results obtained on thin film devices with oxygen vacancies with that of working prototype DSSCs we also measured the photovoltaic parameters of mesoporous DSSC with and without oxygen vacancies. Figure 3.3 and table 3.2 show the IV characteristics and parameters of Vacuum annealed and air annealed DSSCs. It is clear that the air annealed cells have 0.15V more Voc than vacuum annealed cells. Therefore the percentage decrement in the Voc because of oxygen vacancies is 30% whereas corresponding decreased in efficiency is 50%. The photovoltaic parameters are almost recovered after re-annealing vacuum annealed cells in air. In the case of air annealed cells current density is greater than vacuum annealed cell. Importantly the trend in photovoltaic parameters with increased oxygen vacancies is similar to the results obtained with the thin film approach therefore validating the simple thin film approach for the study of basic parameter of DSSC.

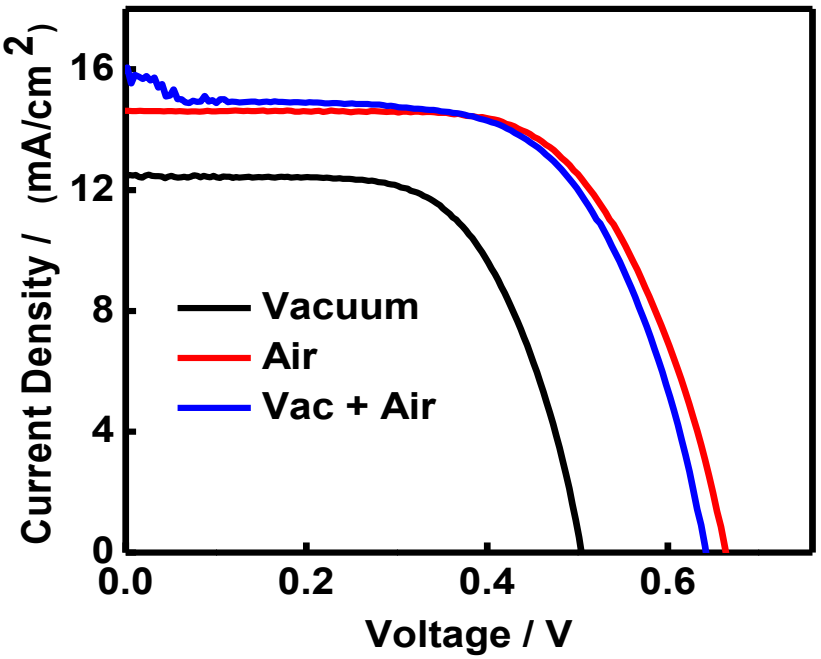

Figure 3.3: J-V characterization of mesoporous TiO_2 DSSC

Parameters	Voc (V)	Jsc (mA/cm^2)	FF	Efficiency
Vacuum Annealed	0.51	13.0	63%	4.2%
Air Annealed	0.66	15.0	64%	6.4%
Vacuum then Air annealed	0.64	15.8	60%	6.1%

Table 1.1: Values of J-V parameters of mesoporous TiO_2 Dye Sensitized Solar Cells

3.3.3 Electrochemical Impedance Spectroscopic Measurements:

To get further insight into the electronic properties of these devices we have done the electrochemical measurements. The chemical capacitance represents the variation in the electron density of states (DOS) as a small variation of applied potential. The chemical capacitance per unit volume is given by

$$C_\mu = e^2 \frac{\partial N_i}{\partial \mu_i}$$

Here the chemical capacitance is defined locally, in a small volume element, and in this interpretation the capacitance reflects the capability of a system to accept or release additional carriers with density N_i due to a change in their chemical potential, μ_i. The chemical capacitance C_μ accounts for the energy storage by virtue of carrier injection. Figure 3.4 (a) shows Cμ of vacuum annealed cells is nearly 10 times higher than that of air annealed cells. The change in chemical capacitance in case of vacuum annealed cells can be attributed to increased density of trap states with increased oxygen vacancies. This is also verified afterwards by charge extraction measurements using transient opto-electronic setup. The increased density of trap states can lead to decreased Voc due to increased recombination rate at TiO_2 electrolyte interface. This is further verified by the lifetime vs voltage and charge transfer vs voltage measurement as shown in Figure 3.4 (b) and (c). [22-26]

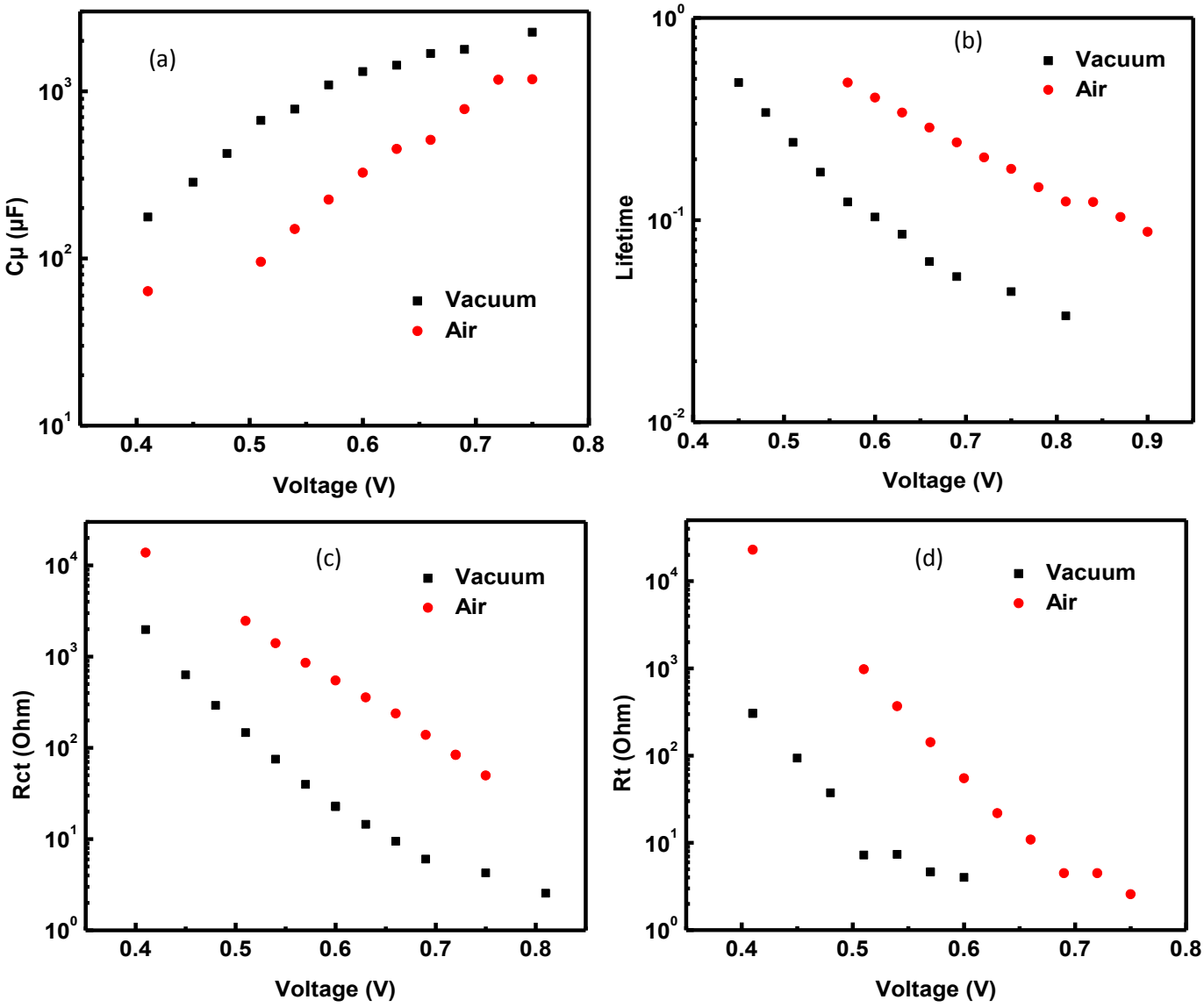

Figure 3.4: Variation of impedance Parameters (a) Chemical Capacitance (Cμ), (b) Lifetime, (c) Recombination Resistance (Rct) and (d) Transport Resistannce (Rt) against Applied Bias Voltage.

Charge transfer resistance (Rct) is a resistance for recombination. Higher R_{ct} indicates an increased electron lifetime, due to lowering of electron and I_3^- (oxidising specie of the electrolyte) recombination. Hence higher will be the photon to electron conversion efficiency. From Figure 3.4 (c), R_{ct} of AA cells is higher by nearly 10 times. Higher the R_{ct}, lower would be the recombination at TiO2-electrolyte interface. Hence the recombination in case of AA is lower by an order of magnitude. This decreased recombination rate in AA case is also reflected in Figure 3.4 (b). Figure 3.4 (d) shows that, Air annealed cells have higher Rt, than vacuum annealed cells. The R_t corresponds to charge transport resistance which should be lower for efficient

charge transport through the TiO_2. Therefore the lower charge transport resistance in case of vacuum annealed case corresponds to efficient carrier transport in these DSSCs. The better transport in case of oxygen deficient TiO_2 can be attributed to higher conductivity caused by oxygen vacancies which act as shallow donor levels in TiO_2. In order to correlate the results obtained by impedance spectroscopy we also carried out the photo-transient measurements to independently obtain the recombination and transport properties.

3.3.4 Optoelectronic Transient Measurement:

The photo transient measurements are interpreted with the multiple trapping continuum model which describes electrons in a semiconductor with an exponential distribution of trapping states. Figure 3.5 show the trap states distribution below conduction band edge. The density of trap states increase exponentially with increase in the electron energy. Nearly 90% of the charges injected into the TiO_2 are trapped in these trap states and only 10% are available in the conduction band. The diffusion in TiO_2 is a result of trapping and de-trapping of conduction band electrons. The nature of these trap levels is not completely understood and it's still an area of active research in semiconductor physics. Hence its effect on semiconducting photovoltaic devices is very difficult to understand.

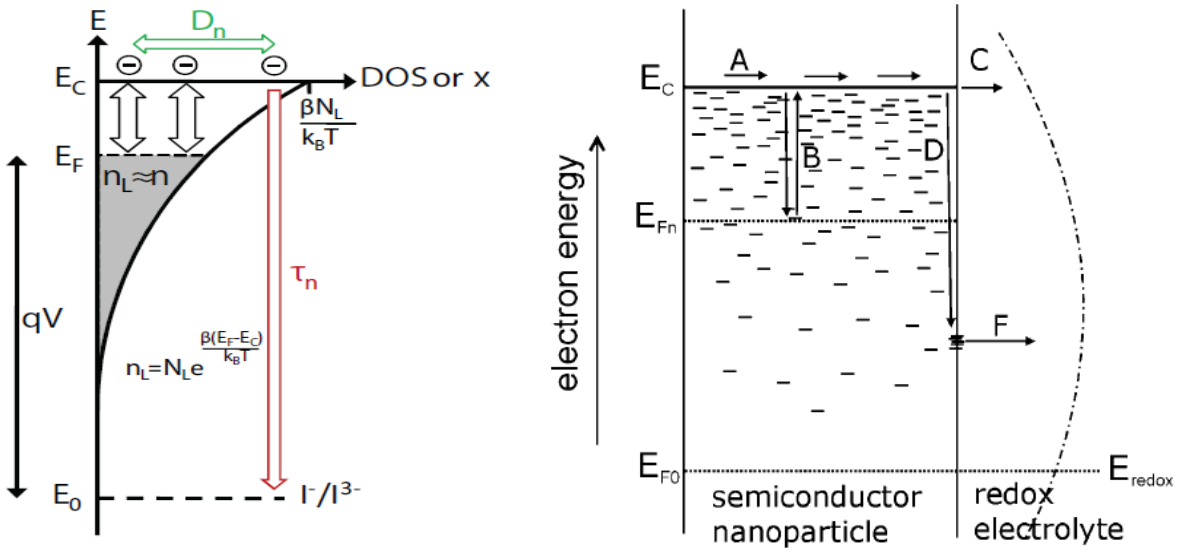

Figure 3.5: Exponential Distribution of trap state density below conduction band edge

To understand the strong dependence on device operating conditions of both the transport and recombination time constants it is generally very helpful to measure the internal charge concentration of a DSSC by charge extraction measurement. Variation in the exponential distribution of trap states with change in photovoltage is shown in Figure 3.6. A clear exponential distribution of charge density with photovoltage can be seen in Figure 3.6. This exponential variation of charge density with photovoltage is assigned to an exponential distribution of delocalized trapping states (N_L) below the conduction band edge which are able to accept electrons. This is also the confirmation of multiple trapping model as a means to describe both electron transport and recombination. [20]

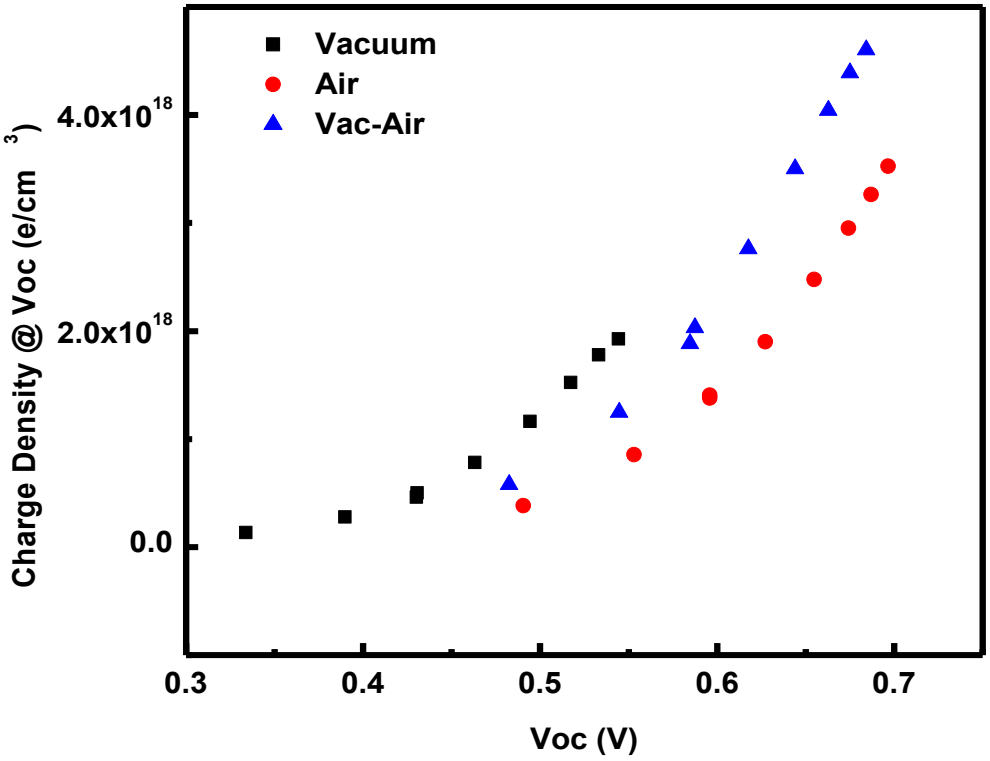

Figure 3.6: Variation of charge density in three DSSC devices against open circuit voltage

The interpretation of transient optoelectronic parameters can possibly done considering shift in conduction band edge or increased trap state density or both. In any case various optoelectronic parameters can vary as shown below.

a) Conduction Band edge shift:

As shown in the Figure 3.7 conduction band edge of TiO_2 is shifted, but the trap state density is still same. Hence, lifetime (τ_n) is apparently increased with respect to photovoltage. However the total charge density remains same. Various graphs obtained with the transient optoelectronic measurements for the case of shift in conduction band edge are shown in Fig. 3.7.

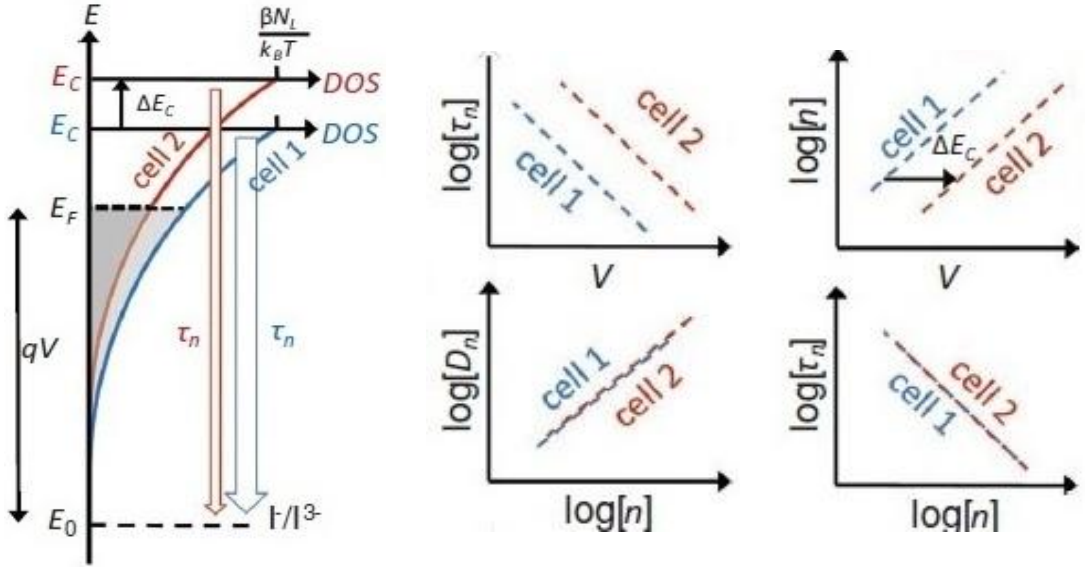

Figure 3.7: Shift in Conduction Band Edge of TiO_2

b) Change in distribution of trap state density

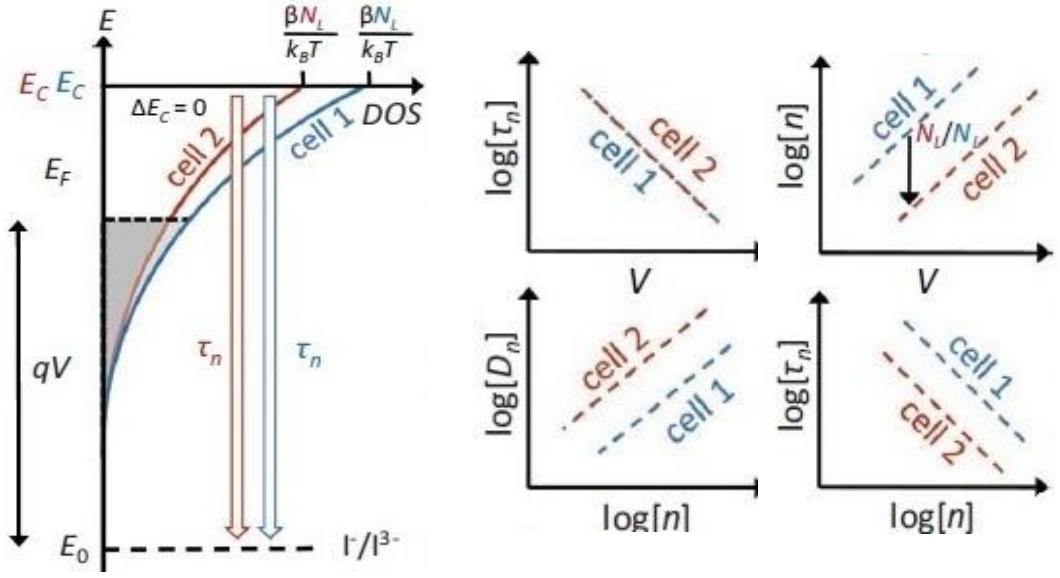

Figure 3.8: Change in Density of Trap States

As shown in the Figure 3.8 trap state density is changed, assuming no shift in TiO_2 conduction band edge. Total charge density is decreased attributed to fewer trap states (vertical shift in charge density with respect to open circuit voltage). For this case lifetime (τ_n) is same for both kind the cells.

Liquid electrolyte dye sensitized solar cells rely on electron diffusion to collect electrons from the porous semiconductor phase in order to generate a photocurrent. The electron transport is mainly through diffusion rather than the drift. [20] The current density j is related to the electron concentration gradient perpendicular to the substrate in the semiconductor by a form of Fick's law:

$$j = -e * D_n * \frac{\partial n}{\partial x}$$

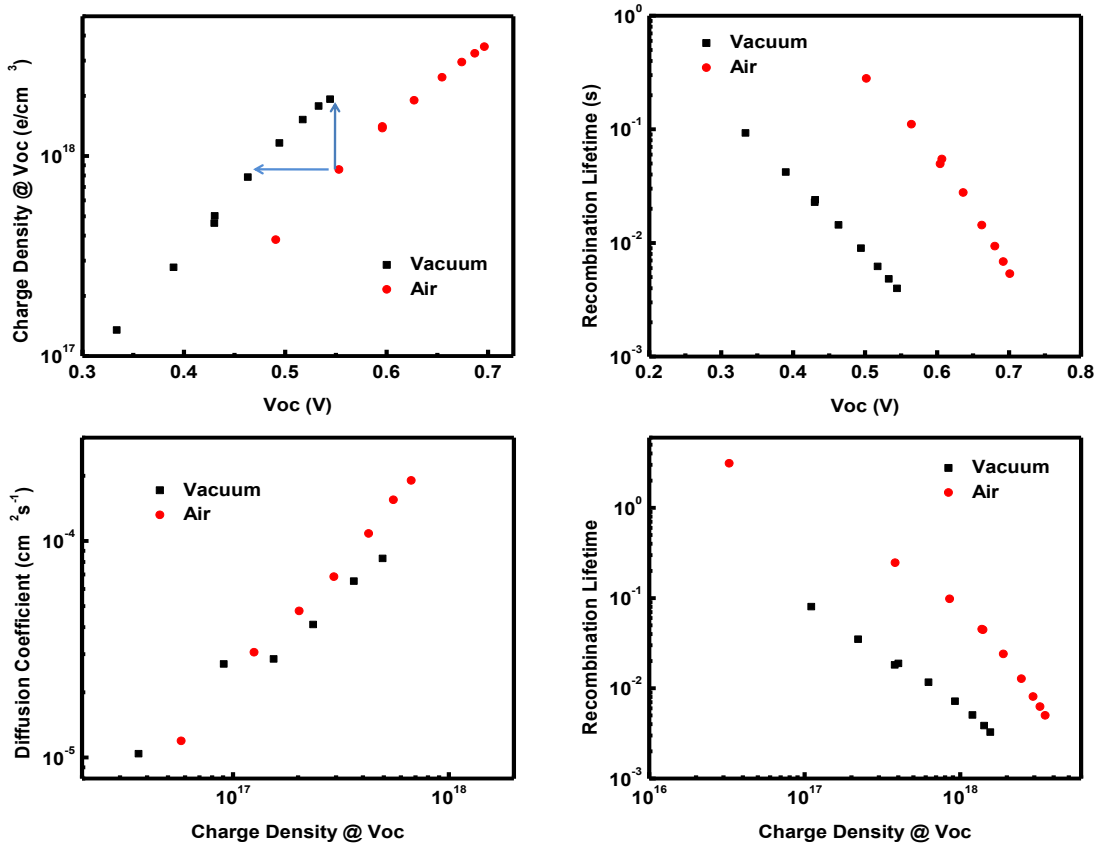

Figure 3.9: (a) Current Density (n) and (b) Recombination Lifetime (τ_n) (c) Diffusion Coefficient (D_n) of Air annealed and (d) Vacuum annealed Dye Sensitized Solar Cells.

The diffusion coefficient can be calculated as

$$D_n = \frac{d^2}{2.47}\left(\frac{1}{\tau_j} - \frac{1}{\tau_n}\right)$$

Where τ_n is electron recombination lifetime and τ_j is electron transport lifetime.

Figure 3.9 shows the various graphs obtained by transient optoelectronic measurements of vacuum annealed (VA) and air annealed (AA) DSSCs. Comparing the various transient graphs of VA and AA cells with that of two cases shown in Fig. 3.7 and Fig. 3.8 it can be concluded that the vacuum annealing should result in both effects viz. shift in conduction band edge as well as increased trap state density due to oxygen vacancies. Fig. 3.9(b) shows that the recombination lifetime of air annealed cells is almost one order higher than the recombination lifetime of vacuum annealed cells. This is also in well agreement with the results obtained from impedance spectroscopy. In order to verify whether the effect of vacuum annealing is recoverable after re-annealing in air we also carried out the transient measurements of the cells which were first annealed in vacuum and then reannealed in air (VAA).

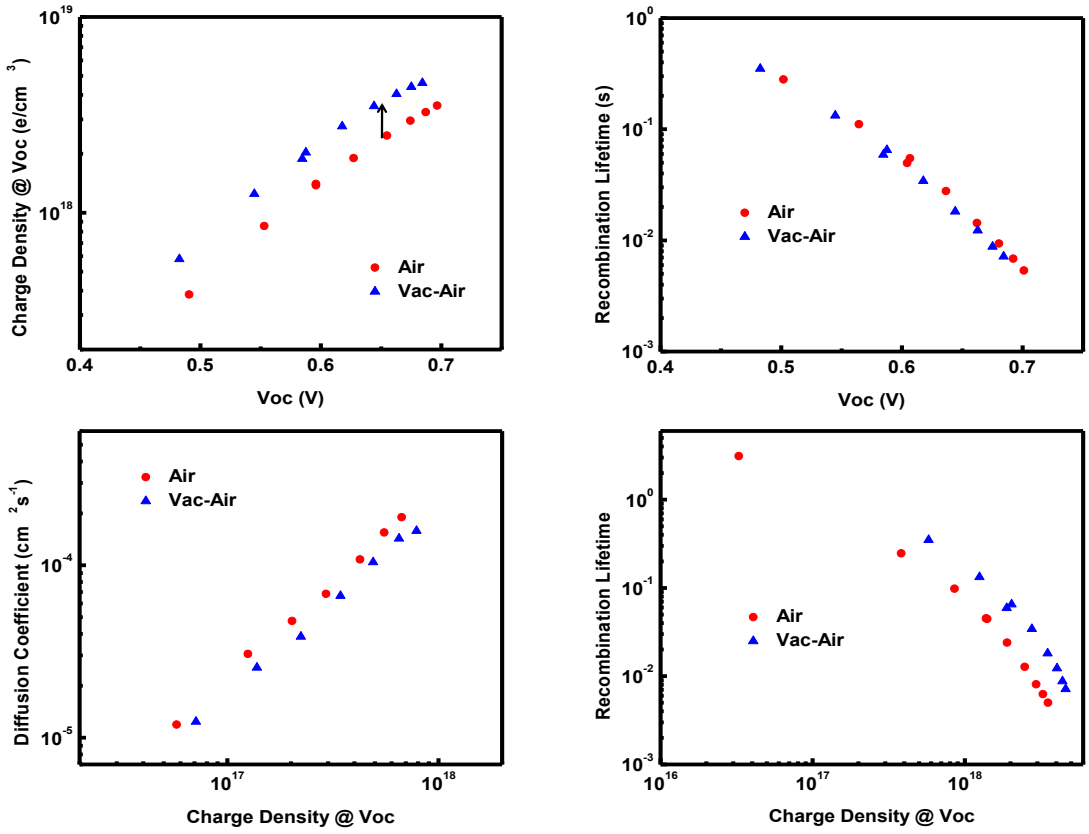

Figure 3.10: (a) Current Density (n) and (b) Recombination Lifetime (τ_n) (c) Diffusion Coefficient (D_n) of Air annealed and Air re-annealed Dye Sensitized Solar Cells.

Figure 3.10 shows various transient optoelectronic parameters of AA and VAA cells. The transient graphs of AA and VAA case are similar to the case shown in Fig. 3.8 which deals with the change in trap density without change in the conduction band edge. From the charge density vs photovoltage graph, it can be concluded that the charge density has upward shift for VAA cells.

Importantly Fig. 3.9 and Fig. 3.10 can distinctly show the difference in the surface oxygen vacancies and bulk oxygen vacancies. When the TiO_2 substrate is annealed in vacuum, oxygen vacancies are created on its surface as well as in the bulk of the TiO_2. However, when re-annealed in air these surface oxygen vacancies have been filled retaining some of the bulk oxygen vacancies. Hence, we conclude that the bulk oxygen vacancies are responsible for change in trap state density but they do not contribute to the conduction band edge shift. Whereas the surface oxygen vacancies are predominantly responsible for conduction band edge shift, but their contribution to change in trap state density cannot be measured from this analysis. The temperature dependant transient analysis can further elucidate this.

The downshift in conduction band edge can be due to the structure of dye after its adsorption to oxygen vacancy sites of TiO_2 or could be due to the interaction of electrolyte with surface oxygen vacancies TiO_2. In order to further evaluate the origin we prepared TiO_2 based photo-electrochemical cells without dye.

3.3.5 Summary

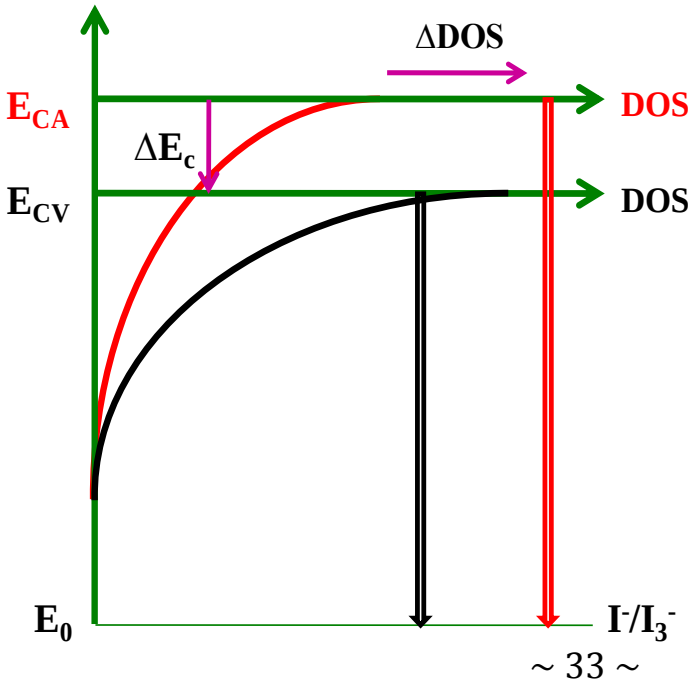

Color Code:
Red = AA Cells
Black = VA Cells

Figure 3.11: The VA cells have dual effect; i.e. VA cells have more number of density of states compared to the AA cells as well as they are the reason for the downshift of the conduction band edge.

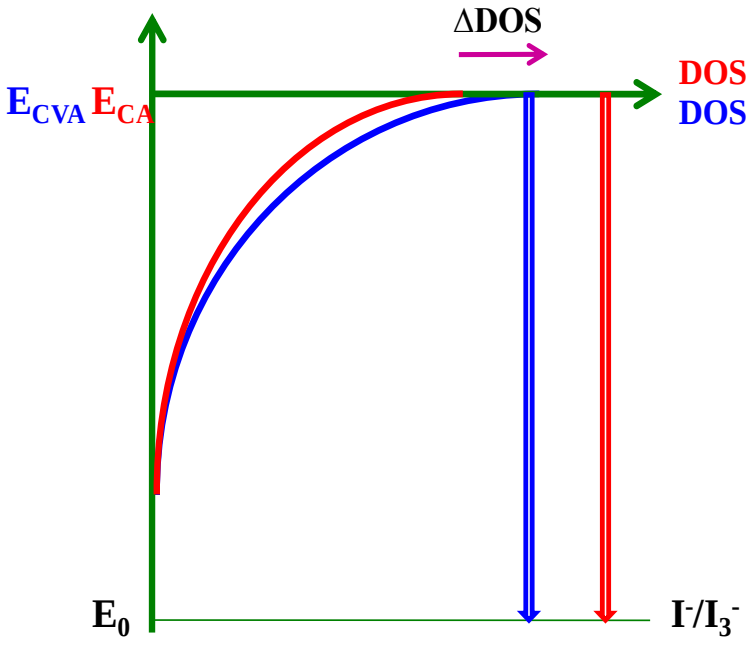

Color Code:

Red = = AA cells

Blue = VAA Cells

Figure 3.12: The VAA cells have no effect on the conduction band edge shift but they are responsible for the increase in the density of states with respect to the AA cells

3.3.5 Electrolyte TiO_2 interface study:

To study the effect of oxygen vacancies and electrolyte interface on conduction band edge shift of TiO_2 in the same DSSC environment, we prepared TiO_2 based photo-electrochemical cells without dye molecules. The cells were fabricated using the same technique, in the absence of dye.

J-V Characteristics:

Parameters	Voc (V)	Jsc (mA/cm^2)	FF	Efficiency
Air Annealed	0.51	0.31	65%	0.10%
Vacuum Annealed	0.37	0.56	60%	0.12%

Table 3.3: Parameters of J-V Curves without dye loading

The JV curves of vacuum annealed and air annealed cells without dye are shown in Fig 3.11. It can be seen that the open circuit potential for vacuum annealed cells without dye also shows the decrease in Voc which is similar to the case of DSSC with dye. The decrease in Voc can mainly be attributed the interface between oxygen deficient TiO_2 and electrolyte which can lead to downshift the conduction band edge and hence give enhanced recombination at this interface. Note that the photo-electron in CB of TiO_2 is not an injected electron from dye it is the photo generated electron in mesoporous TiO_2 due to UV excitation in the solar spectrum. Thus the case of TiO_2 based photo-electrochemical solar cell point out the TiO-electrolyte interface as the origin of decreased Voc in oxygen deficient TiO_2 based DSScs. In order to further understand the transport and recombination dynamics of undyed TiO_2 cells we also carrid out the electrochemical impedance spectroscopy of undyed VA and AA cells.

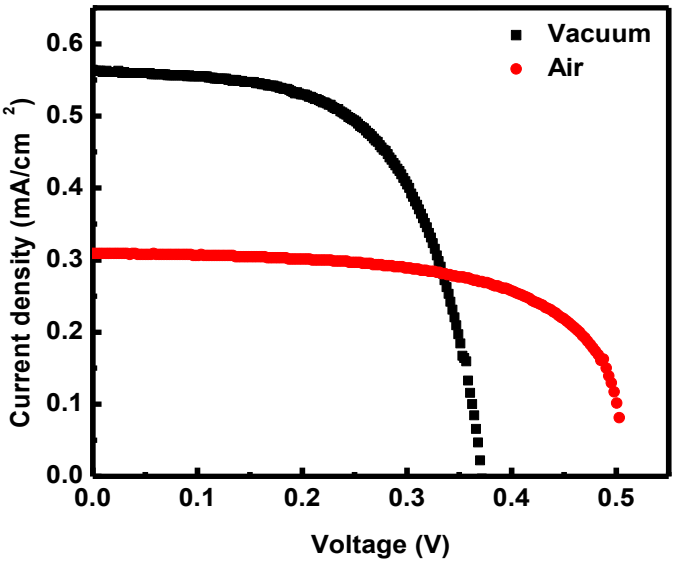

Figure 3.11: J-V Characteristics of VA and AA cells without dye loading

Impedance Analysis

Figure 3.12 shows that transport resistance of VA cells is lower by two orders of magnitude. This drastic difference is due the increased conductivity of TiO_2 samples with oxygen vacancies. Also the diffusion coefficient of VA cells is greater by three orders of magnitude. This supports the high Jsc values for undyed VA cells.

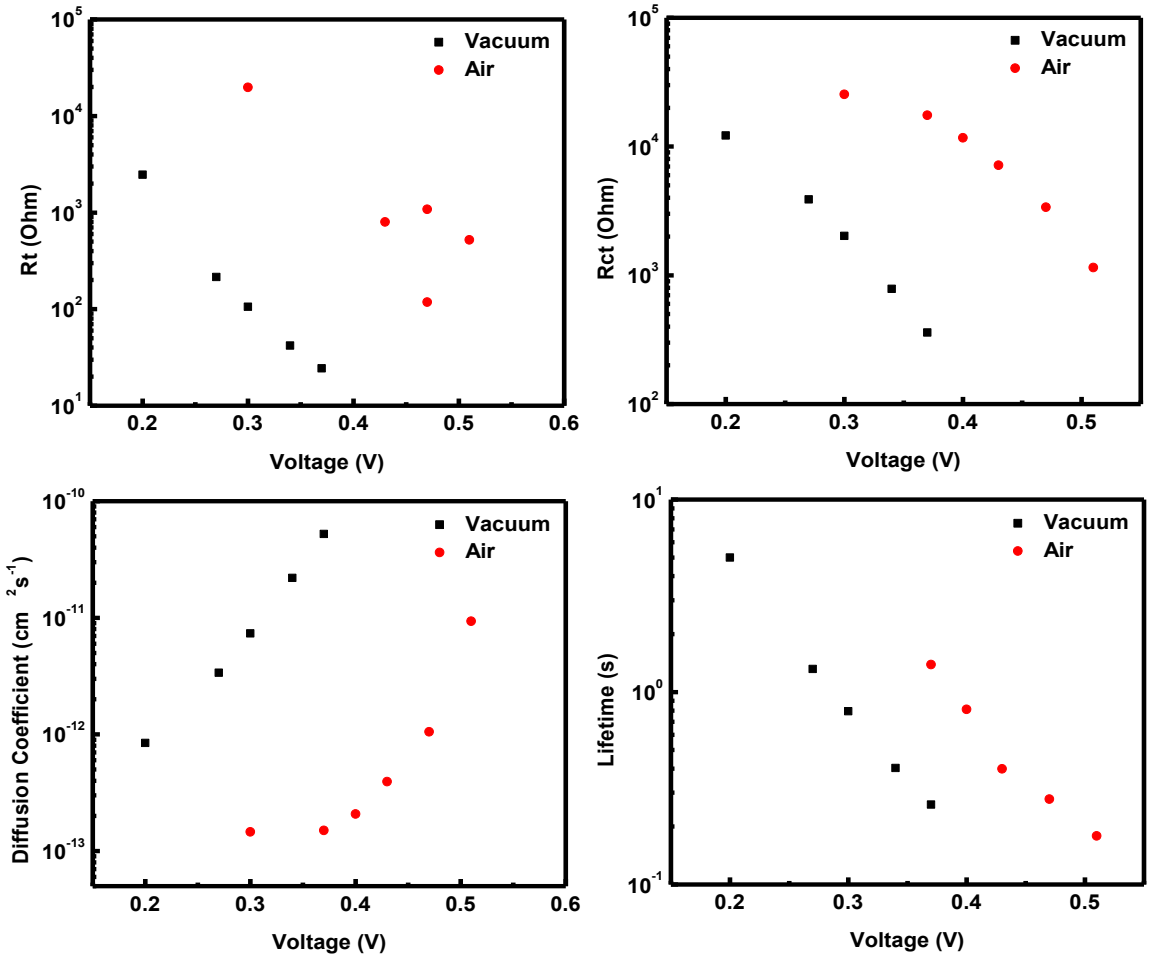

Figure 3.12: Impedance Parameters of Air and Vacuum Annealed cells without dye.

However charge transfer resistance is larger for AA cells by nearly 15 times. It supports the higher recombination in the case of VA cells, which in terns lead to the lower Voc. Although diffusion coefficient is very large for VA cells compared to AA cells, lifetime of AA cells is more than VA cells.

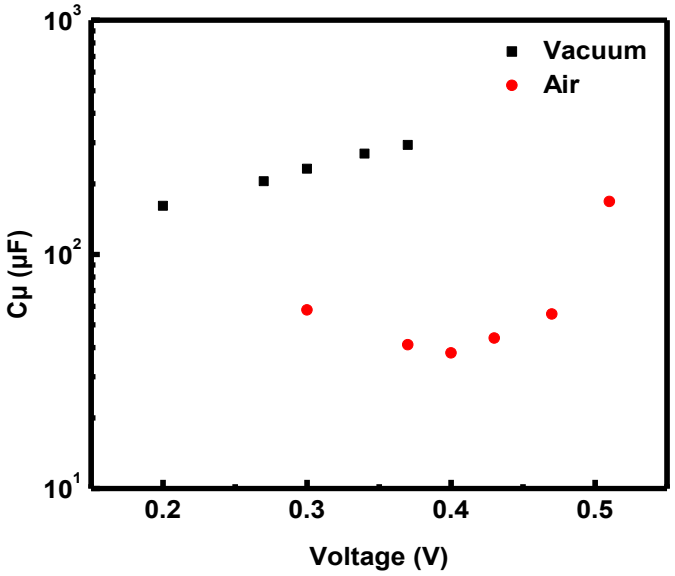

Figure 2.13: Chemical capacitance of undyed solar cells

Chemical Capacitance is shown in figure 3.13 below. It is higher for VA cells than AA cells, which shows that the trap state density is higher for VA cells.

3.4 Conclusion:

In conclusion we systematically studied the effect of oxygen vacancies in TiO_2 on performance of DSSC. It was observed that the oxygen vacancies can lead to interband states below the conduction band of TiO_2 thereby resulting in increased trap state density and downshift of conduction band edge which results in decrease in Voc. Both impedance and transient analysis of oxygen deficient TiO_2 and reference TiO_2 based DSSCs show one order of decrease in recombination lifetime in case of oxygen deficient as compared to reference air annealed TiO_2. Importantly we show that oxygen vacancies on surface and bulk of TiO_2 play different roles in photovoltaic performance. The surface oxygen vacancies are mainly responsible for decreased Voc whereas the bulk oxygen vacancies do not directly contribute to recombination at TiO_2-electrolyte interface. The dominant role of TiO_2-electrolyte interface in oxygen deficient case is further confirmed by the JV and impedance characteristics of undyed films. This study should therefore point out that oxygen vacancies on TiO_2 cannot be beneficial for the photovoltaic performance therefore the origin of increased photovoltaic efficiency with metal/non-metal doping in TiO_2 should lie in some other phenomenon rather than oxygen vacancies.

Section B

Chapter 4: 1D nanofibers - Synthesis and Characterization Techniques

4.1 Introduction:

Nanofibers are the fibrous structures of nanometer scale (typical diameter ~ 10nm – 200 nm). They have many advantages over nanoparticles. The higher values of length (L) vs diameter (D) ratio allows very high surface accessibility over nanoparticles or zero dimensional morphologies. They have several amazing characteristics such as superior mechanical performance (e.g. tensile strength and stiffness) in comparison to their weight. Nanofibers can provide better conductivity over nanoparticles due to less number of grain boundaries. Electron diffusion length in nanofibers is superior over nanoparticulate films. These nanofibers are generally highly porous with a large number of nanopores. Hence they are used in many disciplines of science. In addition to above, their most important property is that they can be incorporated with different additives to give many fascinating properties. [27]

Electrospinning is one of the most popular and low cost technique employed to produce nanofibers. It is a bio-inspired technique, inspired by the ability of spiders to produce fibrous structures. It is a very versatile tool to produce 1D nanofibers of metal oxides or polymers. Nanofibers have a variety of applications in energy devices. Nanofibers of metal oxides like TiO_2, ZnO, SnO_2, etc. can be used in optoelectronic devices. Dye sensitized solar cells fabricated using nanofibrous metal oxide electrodes, provided higher solar–electric energy conversion efficiency as reported in recent papers. [28] Fuel cells made with nanofibrous electrodes enable uniform dispersion of catalysts, and thus increase electrocatalytic activity to obtain higher chemical–electric energy conversion efficiency. Carbon based composite nanofibers can be used for charge storage purposes. [29] Other than energy applications, nanofibers are also used for basic understanding of science. Pan Wang et.al demonstrated in a recent paper the application of functionalized polymer nanofibers in the manipulation of light at the nanoscale level. [30]

4.2 Electrospinning:

The term electrospinning stands for electrostatic spinning. An electrostatic potential is applied between a needle and a collector. The droplet is held by its own surface tension at the spinneret tip, until it gets electro-statically charged. When the surface tension of the fluid is overcome by electrostatic repulsion, the droplet becomes unstable, and a liquid jet is ejected forming a Taylor Cone. Solvent gets evaporated leaving behind charged fibers, which are collected on a metal collecting screen.

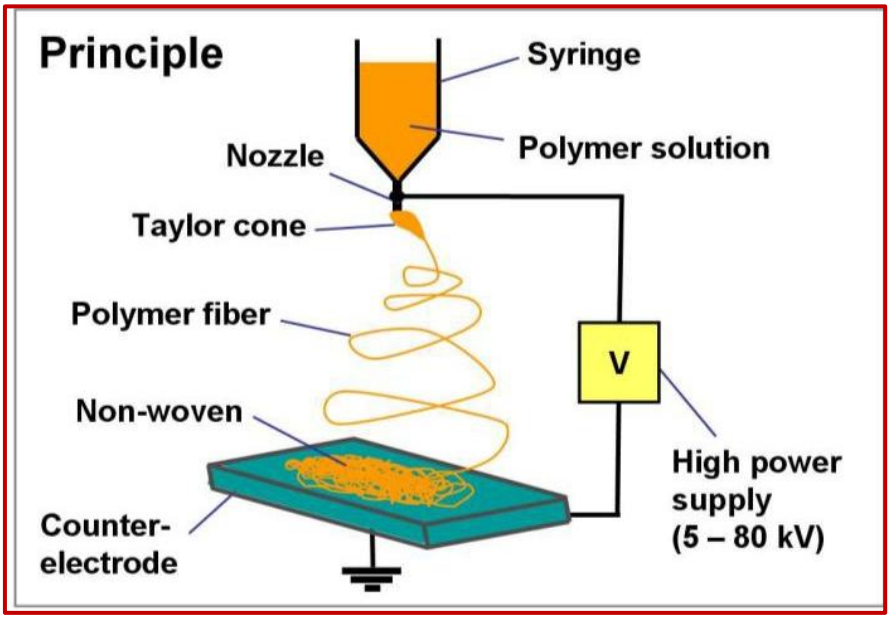

Figure 4.1: Working principle of electrospinning

In electrospinning many parameters are required to be optimized. These parameters can be tuned so as to get fibers with desired properties. The parameters are as follows:

i. Polymer Properties: Molecular weight
ii. Solvent Properties: Surface tension
iii. Solution Properties: Viscosity, elasticity, conductivity
iv. Diameter of the syringe needle
v. Flow rate of the solution (0.1 – 2 ml/hr)
vi. Applied DC voltage potential (5 – 40kV)
vii. Distance between needle and collector (5 – 20cm)

viii. Ambient Parameters: Temperature, Pressure, Humidity, etc.

The fiber formation process in electrospinning is mainly dependent on the intrinsic properties of the solution, such as viscosity concentration and conductivity. Polymer when dissolved in the solution swells up and the polymer chain networks open up. This continuous polymer chain network is mainly responsible for fiber formation during electrospinning. Additionally some extrinsic parameters such as applied potential (kV), distance (cm), and flow rate (ml/hr) also affect the morphology of polymer nanofibers. This technique is useful for making nanofibers of inorganic oxides, which otherwise do not have one dimensional crystal growth. In case of metal oxides, the polymer solution is mixed with the metal oxide precursors and then electrospun to get a fibrous template which can be further calcined to remove the organic part.

4.3 Experimental and Characterization Techniques:

4.3.1 Scanning Electron Microscopy (SEM):

Scanning Electron Microscopy allows direct observation of topography and morphological features. The images are produced by scanning the samples with a focused electron beam. When the electron beam impinges on the specimen, two types of signals are used for imaging purpose namely back scattered electrons and secondary electrons. Back scattered electrons are those which are scattered at 180^{o} angle, when they interact with positively charges nucleus. Secondary electrons are loosely bound electrons, which are released from the sample, when high energetic electrons are incident on the sample. Both these type of electrons are used in SEM for imaging.

4.3.2 Transmission Electron Microscopy (TEM):

In this technique, a beam of electrons is transmitted through an ultra-thin specimen. The image is a result of the interaction between transmitted electrons and the specimen. The image is focused on either a fluorescent screen or a photographic film. Resolution power of TEM is better than SEM. TEM is a very useful technique to capture chemical and electronic information at sub nanometer scale. High resolution

TEM is used to observe crystalline nature of the sample. The d-spacing obtained from TEM can be matched with XRD to determine the crystal phase of the sample.

4.3.3 X-ray Diffraction (XRD):

X-ray crystallography is a very crucial tool for studying properties of crystals. XRD is primarily used for the phase identification of the crystalline material. XRD patterns are generated from the interference patterns of elastically dispersed X-ray beams by atoms. In the XRD instrument, a collimated monochromatic beam of X-rays is incident on the sample. A constructive interference occurs only for certain θ's, for which path difference is an integral multiple of wavelength, given by Bragg's Diffraction Law:

$$2d \sin\theta = n\lambda$$

Where d is the interplanar distance, λ is wavelength of incident X-rays, θ is a scattering angle, and n is the order of diffraction, which is an integer number.

4.3.4 Raman Spectroscopy:

It is a useful tool to analyze the structural/morphological properties of solid oxides. It is an inelastic scattering of light when interacted with molecules. The monochromatic laser light interacts with molecular vibrations, which results in up or down shift in the energy of the photon. The intensity of Stokes or Anti-Stokes is very less as compared to the intensity of Reyleigh Scattering. Hence the wavelengths close to Releigh Scattering are filtered out while the rest are collected on the detector.

4.3.5 Diffuse Reflectance Spectroscopy (DRS):

It is a UV-Visible spectroscopic technique operated in transmittance mode. DRS tells about spectroscopic absorption of light due to electronic transitions. In semiconductors, when the incident photon energy exceeds the band gap energy of the materials, valance band electrons are excited to the conduction band. This gives a sharp dip in the absorption spectrum, which is helpful in finding the band gap of a semiconducting material.

4.3.6 Electrochemical Measurements:

A) Cyclic Voltametry (CV) measurement:

It is a potentiodynamic electrochemical measurement. It is used basically to study cyclic stability of EDLCs or supercapacitors. In this measurement, the working electrode potential is increased at a fixed rate to a maximum set potential and then decreased at the same rate. The current at working electrode is plotted against applied voltage to give a cyclic trace.

B) Cyclic Charge Discharge (CCD) Measurements:

It is a technique employed to determine the cycle life and the capacitance of EDLCs or supercapacitors. It is conducted at a constant current per gram of a sample. From the discharge curve capacitance can be calculated.

4.3.7 High Temperature Pyrolysis:

Pyrolysis is derived from the Greek word pyro (fire) and lysis (separating). It is a thermo-chemical decomposition of materials at high temperatures in an inert atmosphere of N_2 or Ar. It is a concurrent change of chemical composition. It is an irreversible process. It is very often used for the synthesis of carbon materials. In this process samples are heated in an inert atmosphere to very high temperatures (1000^oC), to form graphitized Carbon.

Chapter 5: Au-TiO_2 Nanofibers as a scattering layer in Quantum Dot Sensitized Solar Cells

5.1 Quantum Dot Solar Cells (QDSC)

As discussed in Section-A, QDSC are the semiconductor sensitized solar cells. Quantum Dot Solar Cells are based on a principle of multiple exiton generation. [31] Unlike the third generation dye sensitized solar cells, where single photon leads to single exciton generation, in QDSC a single photon interacts to form an electron hole pair which further interacts to give multiple exciton generation (MEG). MEG may considerably increase the energy conversion efficiency of nanocrystal based solar cells, though extracting the energy may be slightly difficult because of the short lifetimes of these excitons.

5.2 Origin of the problem:

In photovoltaics, use of nanostructures of high electron density metals such as gold or silver is a very hot research topic. It is associated with the plasmonic effect and light scattering phenomenon, charge transfer and local field enhacement. [32-35] Optical scattering and absorption can be manipulated in a controlled fashion over the visible spectrum by these metal nanostructures.[35] The theoretical value of photon to current conversion efficiency of these solar cells is more than 60%, however maximum efficiency achieved is only 5% till today. We believe that light scattering as well as the plasmonic effect can lead to large amounts of light harvesting, which in turn can bring a high increment in the performance of these solar cells.

5.3 Synthesis of Au-TiO_2 nanofibers:

1g of polyvinyl pyrrolidone (PVP; mol wt 1,000,000 g mol^{-1}) was dissolved in 8 ml of absolute ethanol. After complete dissolution, 10µL of conc. HNO_3 was added. 2 mL of titanium tetra-isopropoxide (TTIP) was added to the final solution. The solution was subjected to a high electric field of about 10kV with the tip to collector distance of about 10 cm and the flow rate was maintained at 1ml/hr for electrospinning. The

composite fibers thus obtained were dried in an oven at 70^0C for 5 hours and then calcined at a heating rate of 1^0C/min to 500^0C, for 2 hours. In order to make Au/TiO_2 composite nanofibers, similar protocol was followed but an ethanolic solution of $HAuCl_4.3H_2O$ was added as the gold precursor after acid addition. The ratio of Au:Ti was kept fixed as 1 mol% in the final solution. Thus the Au NPs grew in situ in TiO_2 fibres. [28]

5.4 Device Fabrication:

Here we followed a standard device fabrication technique for QDSC. 8 µm film of TiO_2 was prepared by doctor blading technique. On top of it, a thick 8 µm layer of Au-TiO_2 nanofibers was coated by doctor blading technique. All the films were treated with $TiCl_4$ for pore filling. Then we followed Successive Ionic Layer Adsorption Reaction (SILAR) [36] method for deposition of ex-situ grown quantum dots. In SILAR method films were dipped in the ionic solutions of cadmium and sulphur precursors to adsorb CdS on TiO_2 substrates.

Sensitizer material most commonly used is CdS/CdSe. [37, 38] Although I^-/I_3^- has shown very good performance in DSSC, iodine from the solution causes corrosion to the semiconducting QDs. Hence a new electrolyte used for QDSC is aqueous polysulphide electrolyte (S^{2-}/S_n^{2-}). [39-41] Counter electrode for QDSC is not Pt because of its poor catalytic activity at the photoanode. Therefore a better counter electrode Cu_2S is used for QDSC. [42]

5.5 Results and Discussion:

5.51 TiO_2 and Au-TiO_2 nanofiber Characterisation:

Figure 5.1(a) and 5.1(b) show SEM images of TiO_2 and Au-TiO_2. The fibers synthesized are very smooth, porous and have formed uniform mesh of TiO_2 NF. Fiber diameter is around 150nm with a deviation of few nm. Concentration of gold is very low, just 1mol% with respect to TiO_2 in Au–NF fibers. Hence after electrospinning gold nanoparticles are uniformly distributed without getting agglomerated. This is how gold-TiO_2 composite nanofibers are formed by in situ method after calcination. Figure 5.1(e) and 5.1(f) show high resolution (HR-TEM) images of TiO_2 and Au-TiO_2. Due to crystalline nature of TiO_2 in these nanofibers,

fringes are clearly seen. The darker spots in TEM are due to high Z element. We focused on (200) planes of Au.

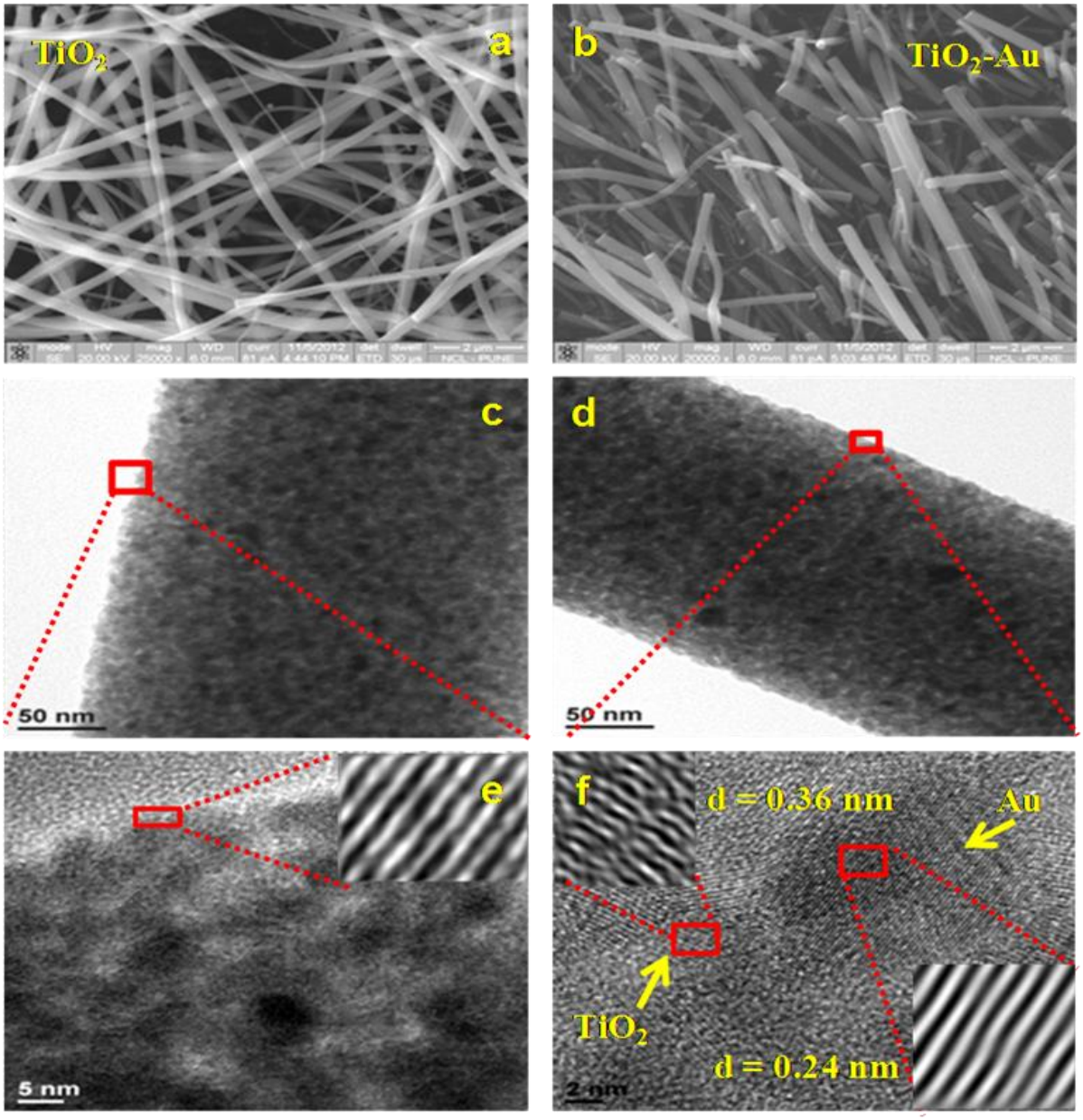

Figure 5.1: SEM and TEM images of TiO_2 NF and Au – TiO_2 NF.

The lattice spacing when measured, we observed d-value to be 0.24 nm, which is a clear indication of Au planes. The d-spacing of other region was found to be 0.36nm, which corresponds to the TiO_2 planes. Hence the uniform distribution of Au nanoparticles in TiO_2 nanofibers was confirmed. The size of Au nanoparticles was in the range of 5-10 nm.

The long range order of structural arrangement is obtained from XRD pattern. More details about imperfections or crystal defects can be observed from more sensitive Raman Spectra. Figure 5.2 (b) shows lower energy E_g mode at 144cm^{-}1, which confirms anatase crystalline phase of TiO_2. The reduced intensity in case of Au-TiO_2 is because of surface adsorbed Au nanoparticles. This result was consistent with XRD pattern. The broadening of diffraction peaks suggest that the strain was

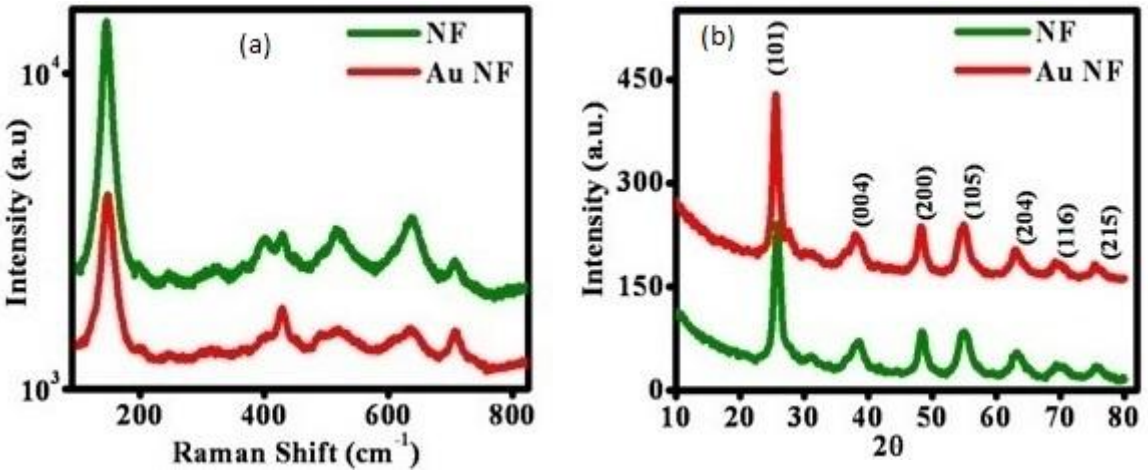

Figure 5.2: (a) Raman and (b) XRD of TiO_2 NF and Au-TiO_2 NF

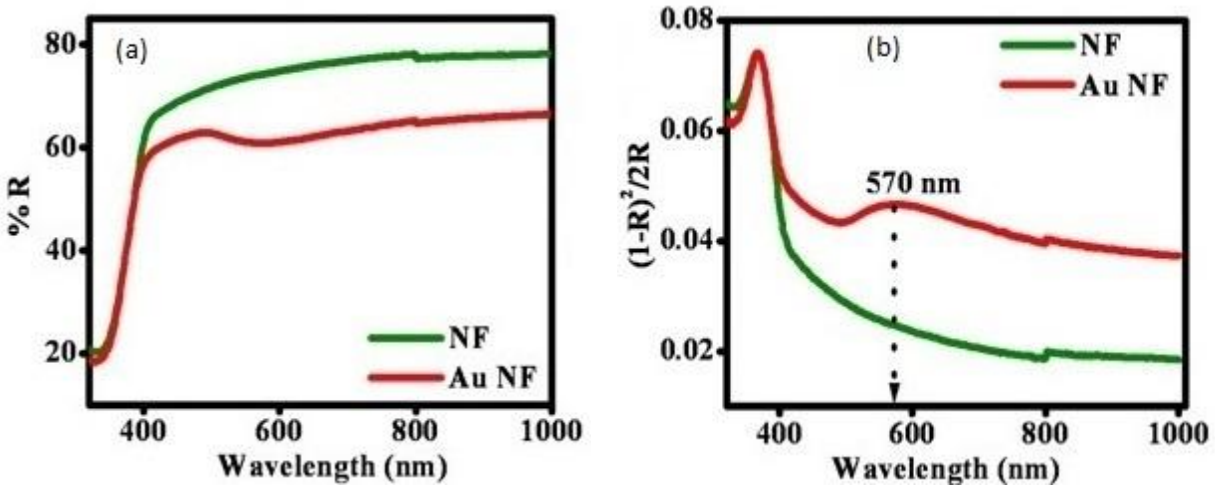

Figure 5.3: Diffuse Reflectance Spectra (DRS) of TiO_2 and Au-TiO_2 NF

induced on TiO_2 framework due to gold nanoparticles. Figure 5.3 shows Diffuse Reflectance Spectra (DRS) of TiO_2 and Au-TiO_2 films without dye loading. Sharp decline in reflectance around 340nm is a consequence of TiO_2 band edge absorption. To observe the plasmonic contribution we have used simple Kubelka–Munk theory. [43] This theory introduces two parameters as S and K, which relate to the strength of scattering and absorption of the fibers. Borensztein et.al. [44] have

stated the relationship of the parameters S and K with the reflectance of the opaque sample recorded in the integrating sphere assembly. The relationship is given by

$$\frac{K}{S} = \frac{(1-R)^2}{2R}$$

The presence of broad peak centered at 570 nm is due to gold nanoparticles, is red shifted compared to usual peak observed around 520-530nm.[45] This indicates better light harvesting ability of Au-TiO_2 over TiO_2 NF in the visible region.

5.5.2 Photovoltaic Charatcerization:

Various characterization methods could conclude the use of gold nanoparticles in the harvesting layer to be beneficial for both; improved light harvesting and enhanced electrochemical performance of the device. Figure 5.4 shows J-V characteristics of the QDSC with active area 0.25cm^2 under standard AM 1.5 simulated sunlight. Table 1 gives recorded J-V parameters. The photon to current conversion efficiency of cells without scattering layer is 2.6%. However with scattering layer of TiO_2 nanofiber efficiency is raised to 3.6% and in Au-TiO_2 nanofiber scattering layer it reaches to as maximum as 4.3%. Increment in efficiency is very high. It is about 38% for TiO_2 nanofiber cells with reference to without scattering layer and a tremendous increment in the efficiency about 65% for Au-TiO_2 nanofibers. This increment is due to a significant enhancement in the short circuit current. Also the fill factor and the open circuit voltage for Au-TiO_2 cells have increased.

Parameters	Voc (V)	Jsc (mA/cm^2)	FF	Efficiency
Without scattering Layer	0.52	12.7	40.4%	2.6%
With TiO_2 NF scattering layer	0.53	16.6	40.5%	3.6%
With Au-TiO_2 scattering layer	0.57	17.8	42.3%	4.3%

Table 5.1: J-V characteristics of QDSC

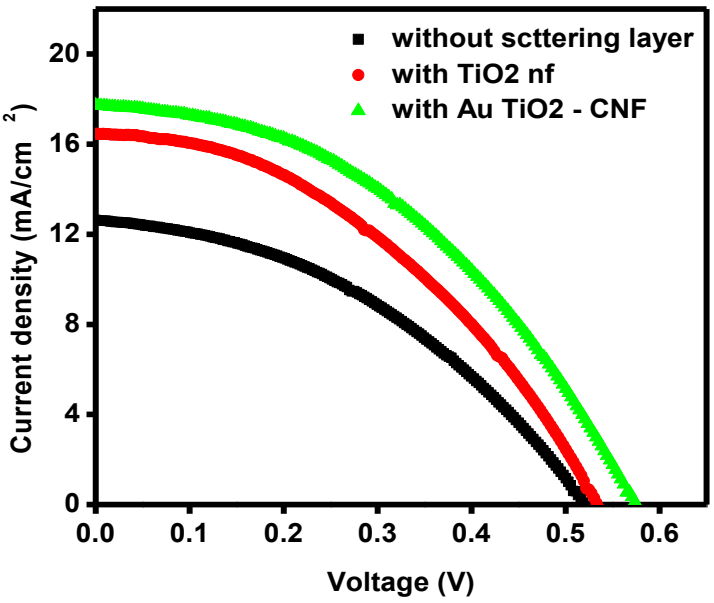

Figure 5.4: J-V characteristic of QDSC

5.6 Conclusions:

We have fabricated Quatum Dot Solar Cells, and demonstrated a significant improvement in the solar cell parameters by using Au-TiO_2 as a light harvesting layer. The gold loaded fibers have shown enhancement in the short circuit current due to their ability to reflect light back to the quantum dot sensitizers.

Chapter 6: $NiFe_2O_4$ - Carbon Nanofibers for Charge Storage Application

6.1 Introduction of Supercapacitors:

Supercapacitors differ from normal capacitors as they have very high capacitance. Supercapacitors have high specific power density which is comparable to the usual capacitors. But they have nearly 100 times more specific energy density. Capacitance of infinite parallel plate capacitor is given as

$$C = \frac{\epsilon A}{d}$$

Where ϵ is the dielectric constant of the medium, A is the effective surface area and d is the separation between opposite charges. As ϵ is a material property it has limitations in its increment. However, a material with high surface area and very small distance between opposite charges can be synthesized. This principle is used in the development of supercapacitors.

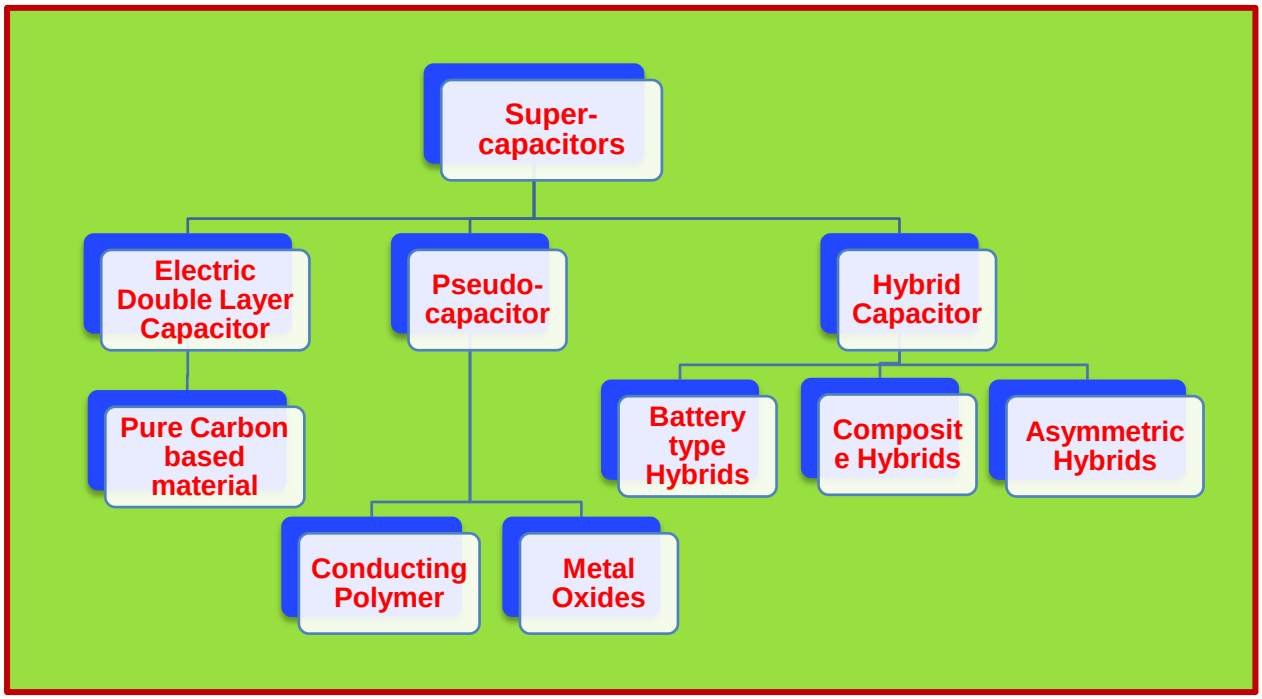

Figure 6.1: Hierarchy of Supercapacitors

Supercapacitors are classified into three major categories. First is electric double layer capacitors (EDLC). They are pure carbon based supercapacitors. Charge strorage is achieved by formation of electrical double layer between the electrode and ions in the electrolyte. This is called as Helmholtz Double Layer. These capacitors have very high surface area and very low “d’. The specific capacitance achieved typically is 100F/g, while the normal capacitors have capacitance in µF. They have high power density.

Electrodes of Pseudocapacitors are generally metal oxides. In psedocapacitors electric charges are stored faradaically, by electron charge transfer between the electrode and the electrolyte. This is accomplished by reduction – oxidation (redox) reactions and intercalation. Charge storage of pseuocapacitors is very high e.g. specific capacitance of RuO_2 is 720F/g, much higher than EDLC.

Hybrid supercapacitors are mostly asymmetric capacitors. They are combination of an electrode with high amount of EDLC and an electrode with high amount of pseudocapacitance. Hence these capacitors can give higher capacitance as well as high energy density.

6.2 $NiFe_2O_4$-CNF for charge storage:

6.2.1 Origin of the problem:

Waldemar Jungner and Thomas Edison invented nickel – iron battery in 1902 [46,47] with Fe as the cathode and Ni as the anode material. Spinel ferrite oxides (MFe_2O_4) are considered as promising scalable alternative materials for high performance supercapacitor applications. However, due to poor conductivity of ferrites, a promising approach towards designing ferrite based hybrids is currently of major interest.

$NiFe_2O_4$ is a kind of hybrid supercapacitor material. Here we report the in situ synthesis of hollow $NiFe_2O_4$ on cabon nanofibers. Same material is used for both electrodes as in the symmetric electrodes, but at cathode only Fe-component would be activated and at anode only the Ni-component. Hence it will act like a asymmetric supercapacitor. Voltage window of this supercapacitor will be from -1.2V to +0.6V total range 1.8V, which is very useful because aqueous based supercapacitors suffer

from narrow operational voltage window of less than 1V due to electrochemical splitting of water. [48,50] Maximum energy achieved by maximum specific capacitance (C) and operating voltage (V) is E= ½ CV^2. It increases quadratically with increase in V. However in this report our focus is mainly on the cathode in a voltage window of 0V to -1.2V.

6.2.2 Synthesis of $NiFe_2O_4$ – carbon nanofibers:

0.4g polyacrilonitrile (PAN) was dissolved in 5ml dimethyleformamide (DMF). Solution was stirred at room temperature for 2 hours. 0.6mmol of $Fe(acac)_3$ and 0.3mmol $Ni(acac)_2$ was added to the solution. Solution was electrospun at a flow rate of 0.3ml/hr with an applied potential of 10kV at 15cm distance. Fibers were annealed at 225^0C for 2 hours and then carbonized at 800^0Cfor 2 hours in N_2 environment at a rate of 5^0C/min. The synthesized product was mildly oxidized at 350^0C for 1 hour. [49]

6.2.3 Electrode Making Protocol:

Electrodes for supercapacitor testing were prepared using the standard protocol for supercapacitor measurement. 75 wt% of NiFe2O4 – CNF was mixed with 20 wt% of conducting carbon (acetylene black) and 5 wt% of PVDF (polyvinylidene fluoride) binder. To the above mixture 4-5 drops of NMP (N-methyl-2-pyrrolidone) were added. This mixture was ground thoroughly to make a uniform viscous slurry. This slurry was coated on toray carbon paper with approximately 1mg loading of active material in 1 cm^2 area. These electrodes were dried in an oven for 12 hours at 90^0C.

6.2.4 Electrochemical measurements:

Electrochemical cyclic voltametric measurements were performed in 1M KOH solution. The measurements were performed in a three electrode system. $NiFe_2O_4$ – CNF electrode was used as a working electrode. Pt as a counter electrode and {Hg |HgO} was used as a reference electrode. Potential window used for CV analysis was from -1.2V to 0V.

Assembly for electochemical charge discharge measurements is the same. The capacitor was charged by constant current to a set potential. Then it was

allowed to discharge by the constant reverse current of same magnitude. This measurement is very useful in calculating the specific capacitance of the sample.

6.3 Results and Discussion:

6.3.1 Material Characterization:

XRD pattern gives information about long range order in the structural arrangement. Figure 6.2 shows XRD of $NiFe_2O_4$- CNF. To calculate lower bound on particle size Scherrer Equation is used:

$$D_p = \frac{0.94\lambda}{\beta_{1/2}\cos\theta}$$

Where D_p is mean size of ordered crystalline domains, θ is a Bragg angle, λ is wavelength of light used, $\beta_{1/2}$ is full width at half maximum (FWHM) of the most intense XRD peak in radians, and 0.94 is due to shape factor. After substituting all parameters (λ = 1.24pm, 2θ = 36.2 and β = 0.8°= 0.014 radians), we get D_p = 87.64pm.

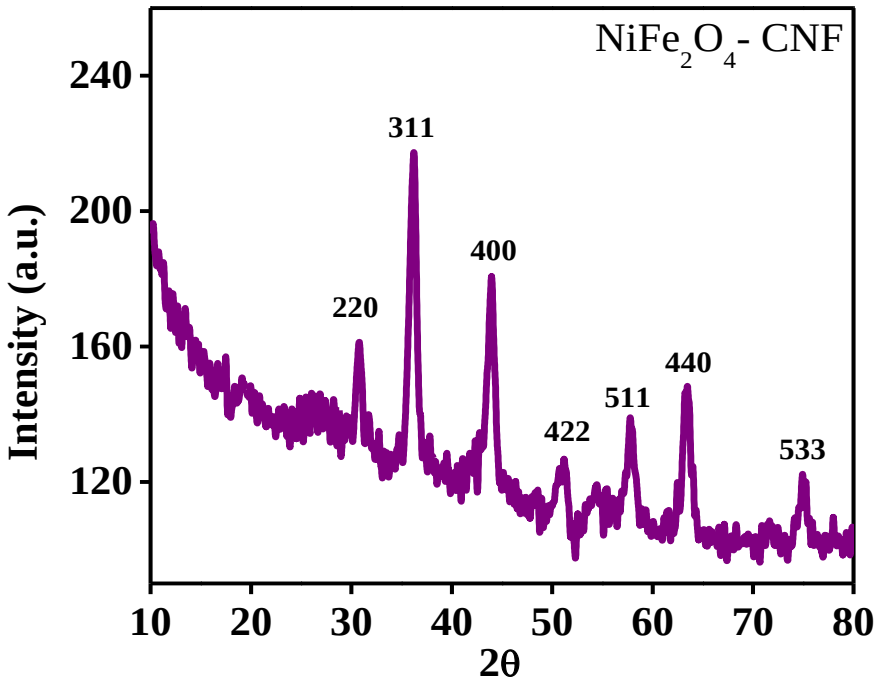

Figure 6.2: XRD of $NiFe_2O_4$, their klm values of major peaks are given

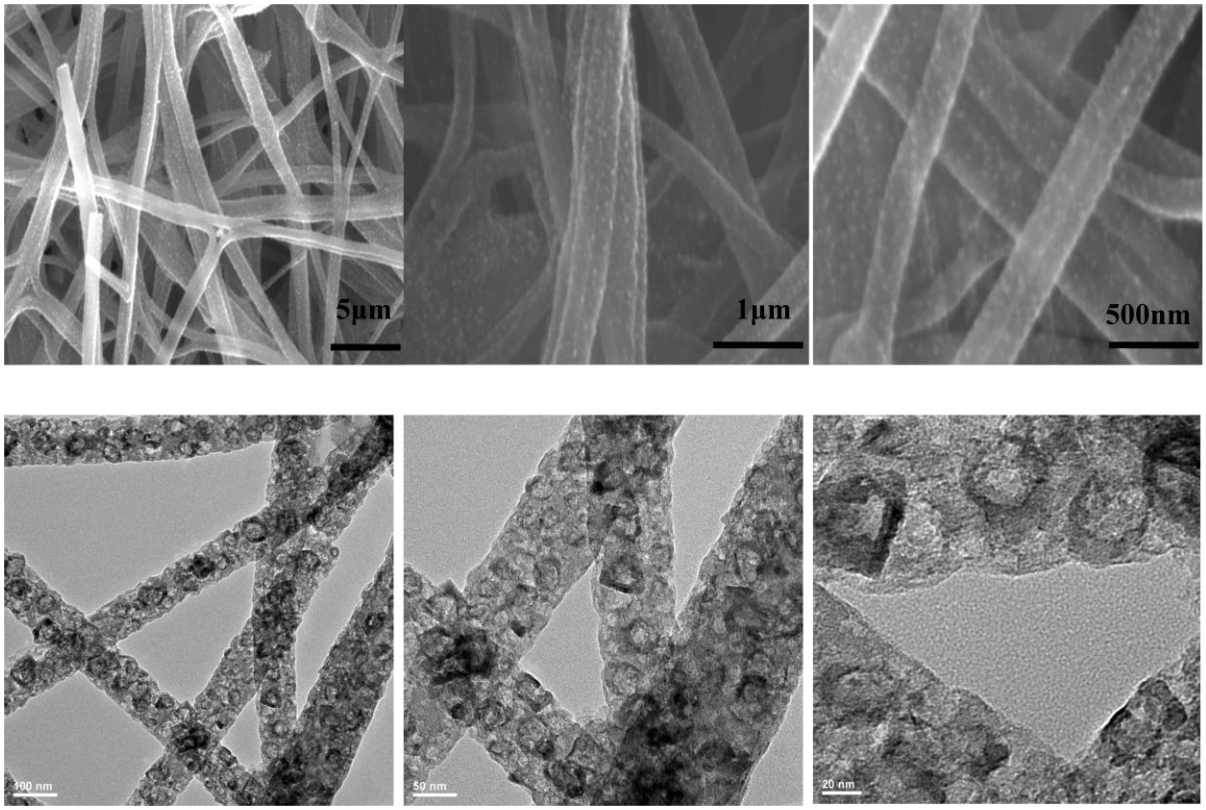

Figure 6.3: SEM and TEM images of $NiFe_2O_4$

The SEM and TEM images of NiFe2O4 – CNF are shown in Figure 6.3. The bright spots on the carbon nanofibers are of $NiFe_2O_4$. These fibers are highly porous nanostructures. The size of the spinal structures has a large variation. There are very tiny nanoparticles (size~5-10nm) as well as large nanostructures (size~100nm). These nanoparticles have a uniform distribution in carbon nanofibers. It is observed that these nanoparticles come to the surface of carbon nanofibers leaving porous CNF from inside.

6.3.2 Electrochemical Measurements:

The cathode of this pseudocapacitor was $NiFe_2O_4$ while we used Pt as a counter electrode. CV curves were taken at different scan rates from 3mV/s to 100mV/s. The CV and charge-discharge curves are shown in the figure. At lower scan rate, enough time was available for faradic reaction to occur. Hence, sharp redox peaks corresponding to reactions mentioned in equation (I) were observed. However, as the scan rate increased, contribution of electrochemical charge storage reduced and EDLC character appeared. Very fast charging and discharging, due to

formation of Helmholtz layer was observed. These two mechanisms contributed to the high specific capacitance.

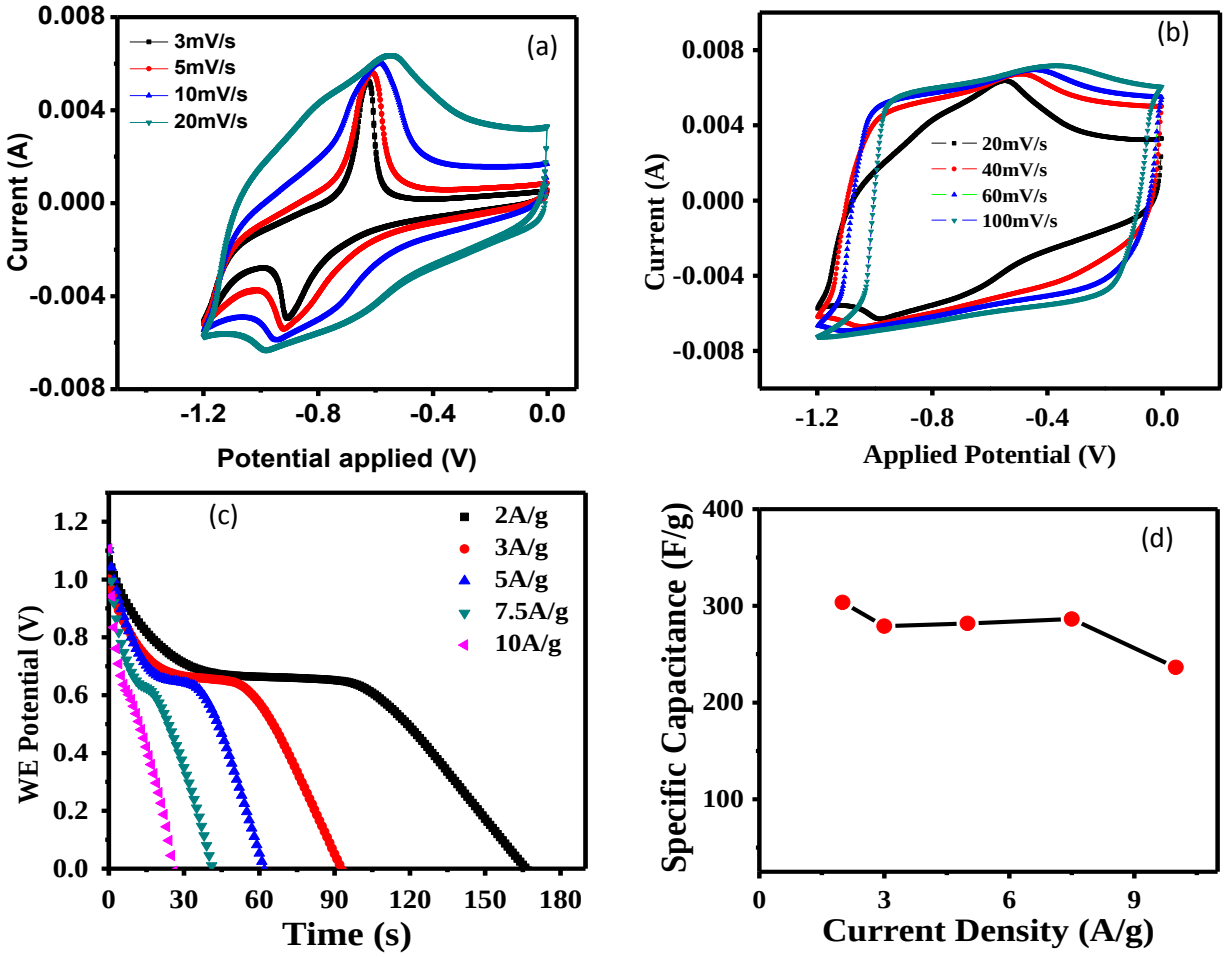

Figure 6.4: (a) CV at lower scan rate, (b) CV at higher scan rate, (c) charge discharge curves, (d) specific capacitance

Figure 6.4(a), shows reduction and oxidation peaks of Fe

$Fe^{3+} + e^- \rightarrow Fe^{2+}$ at -0.9V

$Fe^{2+} \rightarrow Fe^{3+} + e^-$ at -0.6V …….. Equation (I)

The charge is stored in this pseudocapacitor during charging (from 0V to -1.2V) by reduction of Fe^{3+} and it is released during discharging (from -1.2V to 0V) by oxidation of Fe^{2+}. In figure 6.4(b) it is observed that at high scan rate the electric double layer capacitor (EDLC) is contributing to the capacitance. Figure 6.4(c), shows the discharge curves, the plateau is due to the oxide contribution and triangular shaped curve with uniformly releasing charges is due to the contribution from carbon.

The specific capacitance of a capacitor is calculated as:

$$C = \frac{I * \Delta t}{m * \Delta V}$$

Where I is the applied constant current, m is the active mass of the sample, ∆t is the discharge time and ∆V is the set potential. Figure 6.4(d) shows that it has very high specific capacitance at scan rate of 2A/g around 300 F/g. Even at higher current densities such as 8A/g; 90% of the charge storage capacity was retained by this supercapacitor.

6.4 Conclusions:

$NiFe_2O_4$ – carbon nanofibers based electrode shows specific capacitance of 300F/g at current density of 2A/g. Even at higher current densities such as 8A/g almost 90% of retention of capacitance was observed. The flexible composite shows good stability in performance even at higher current rates of charge discharge. This type of hybrid system can be used for asymmetric supercapacitor as it mainly shows very good capacitive performance.

References

Section A:

1. O'Regan, B. C. & Grätzell, M. A low-cost, high-efficiency solar cell based on dye-sensitized colloidal TiO2 films. *Nature* **353,** 737–740 (1991).
2. Catchpole, K. R. *Third generation photovoltaics*. 59–64 (2002). doi:10.1109/COMMAD.2002.1237188
3. Burschka, J. *et al.* Sequential deposition as a route to high-performance perovskite-sensitized solar cells. *Nature* **499,** 316–9 (2013).
4. Ito, S. *et al.* Fabrication of thin film dye sensitized solar cells with solar to electric power conversion efficiency over 10%. *Thin Solid Films* **516,** 4613–4619 (2008).
5. Ito, S. *et al.* Fabrication of Screen-Printing Pastes From TiO 2 Powders for Dye-Sensitised Solar Cells. 603–612 (2007). doi:10.1002/pip
6. Gratzel, M. Solar Energy Conversion by Dye-Sensitized Photovoltaic Cells. **44,** 6841–6851 (2005).
7. Gratzel, M. Photoelectrochemical cells. **414,** (2001).
8. Peter Meisen. A Study of Very Large Solar Desert Systems with the Requirements and Benefits to those Nations Having High Solar Irradiation Potenial. *Global Energy Network Institute (GENI)* July (2006).
9. Fabregat-Santiago, F., Garcia-Belmonte, G., Mora-Seró, I. & Bisquert, J. Characterization of nanostructured hybrid and organic solar cells by impedance spectroscopy. *Phys. Chem. Chem. Phys.* **13,** 9083–118 (2011).
10. Bisquert, J. Theory of the Impedance of Electron Diffusion and Recombination in a Thin Layer. *J. Phys. Chem. B* **106,** 325–333 (2002).
11. Fabregat-Santiago, F., Bisquert, J., Garcia-Belmonte, G., Boschloo, G. & Hagfeldt, A. Influence of electrolyte in transport and recombination in dye-sensitized solar cells studied by impedance spectroscopy. *Sol. Energy Mater. Sol. Cells* **87,** 117–131 (2005).
12. Fabregat-santiago, F. *et al.* Correlation between Photovoltaic Performance and Impedance Spectroscopy of Dye-Sensitized Solar Cells Based on Ionic Liquids. *J. Phys. Chem.* **2,** 6550–6560 (2007).

13. Lagemaat, J. Van De, Kopidakis, N., Neale, N. R. & Frank, A. J. Effect of Electron-Electron Interaction on Transport in Dye-Sensitized Nanocrystalline. (2005).
14. Leng, W. H., Barnes, P. R. F., Juozapavicius, M., O'Regan, B. C. & Durrant, J. R. Electron Diffusion Length in Mesoporous Nanocrystalline TiO 2 Photoelectrodes during Water Oxidation. *J. Phys. Chem. Lett.* **1,** 967–972 (2010).
15. Xing, M., Zhang, J., Chen, F. & Tian, B. An economic method to prepare vacuum activated photocatalysts with high photo-activities and photosensitivities. *Chem. Commun. (Camb).* **47,** 4947–9 (2011).
16. Tian, H. *et al.* Enhanced photovoltaic performance of dye-sensitized solar cells using a highly crystallized mesoporous TiO2 electrode modified by boron doping. *J. Mater. Chem.* **21,** 863 (2011).
17. Zhang, J. *et al.* Increasing the Oxygen Vacancy Density on the TiO 2 Surface by La-Doping for Dye-Sensitized Solar Cells. 18396–18400 (2010).
18. Kim, Y. *et al.* Low-temperature oxygen plasma treatment of TiO2 film for enhanced performance of dye-sensitized solar cells. *J. Power Sources* **175,** 914–919 (2008).
19. Meng, S. & Kaxiras, E. Electron and hole dynamics in dye-sensitized solar cells: influencing factors and systematic trends. *Nano Lett.* **10,** 1238–47 (2010).
20. Barnes, P. R. F. *et al.* Interpretation of optoelectronic transient and charge extraction measurements in dye-sensitized solar cells. *Adv. Mater.* **25,** 1881–922 (2013).
21. Jennings, J. R., Liu, Y., Safari-alamuti, F. & Wang, Q. Dependence of Dye-Sensitized Solar Cell Impedance on Photoelectrode Thickness. *J. Phys. Chem.* 1556–1562 (2012).
22. Bisquert, J. Chemical capacitance of nanostructured semiconductors: its origin and significance for nanocomposite solar cells. *Phys. Chem. Chem. Phys.* **5,** 5360 (2003).
23. Archana, P. S. *et al.* Random nanowires of nickel doped TiO2 with high surface area and electron mobility for high efficiency dye-sensitized solar cells. *Dalton Trans.* **42,** 1024–32 (2013).

24. Carnie, M. J. *et al.* Ultra-fast sintered TiO2 films in dye-sensitized solar cells: phase variation, electron transport and recombination. *J. Mater. Chem. A* **1,** 2225 (2013).
25. Mukherjee, K., Teng, T.-H., Jose, R. & Ramakrishna, S. Electron transport in electrospun TiO_2 nanofiber dye-sensitized solar cells. *Appl. Phys. Lett.* **95,** 012101 (2009).
26. Klahr, B., Gimenez, S., Fabregat-santiago, F., Hamann, T. & Bisquert, J. Water Oxidation at Hematite Photoelectrodes: The Role of Surface States. *J. Chem. Soc.* (2012).

Section B:

27. Thavasi, V., Singh, G. & Ramakrishna, S. Electrospun nanofibers in energy and environmental applications. *Energy Environ. Sci.* **1,** 205 (2008).
28. Naphade, R. a., Tathavadekar, M., Jog, J. P., Agarkar, S. & Ogale, S. Plasmonic light harvesting of dye sensitized solar cells by Au-nanoparticle loaded TiO2 nanofibers. *J. Mater. Chem. A* **2,** 975 (2014).
29. Huang, Z.-M., Zhang, Y.-Z., Kotaki, M. & Ramakrishna, S. A review on polymer nanofibers by electrospinning and their applications in nanocomposites. *Compos. Sci. Technol.* **63,** 2223–2253 (2003).
30. Wang, P., Wang, Y. & Tong, L. Functionalized polymer nanofibers: a versatile platform for manipulating light at the nanoscale. *Light Sci. Appl.* **2,** e102 (2013).
31. Sambur, J. B., Novet, T. & Parkinson, B. a. Multiple exciton collection in a sensitized photovoltaic system. *Science* **330,** 63–6 (2010).
32. Barnes, W. L., Dereux, A. & Ebbesen, T. W. subwavelength optics. *Nature* **424,** 824–830 (2003).
33. Atwater, H. A. & Polman, A. Plasmonics for improved photovoltaic devices. *Nat. Mater.* **9,** 205–13 (2010).
34. Brown, M. D. *et al.* Plasmonic dye-sensitized solar cells using core-shell metal-insulator nanoparticles. *Nano Lett.* **11,** 438–45 (2011).
35. Pillai, S. & Green, M. a. Plasmonics for photovoltaic applications. *Sol. Energy Mater. Sol. Cells* **94,** 1481–1486 (2010).

36. Vogel, R., Pohl, K. & Weller, H. Sensitization of highly porous , polycrystalline Ti02 electrodes by quantum sized CdS. *Chem. Phys. Lett.* **174,** 241–246 (1990).
37. Lee, H. *et al.* Efficient CdSe quantum dot-sensitized solar cells prepared by an improved successive ionic layer adsorption and reaction process. *Nano Lett.* **9,** 4221–7 (2009).
38. Hodes, G. Comparison of Dye- and Semiconductor-Sensitized Porous Nanocrystalline Liquid Junction Solar Cells. *J. Phys. Chem. C* **112,** 17778–17787 (2008).
39. Shalom, M., Tachan, Z., Bouhadana, Y., Barad, H. & Zaban, A. Illumination Intensity-Dependent Electronic Properties in Quantum Dot Sensitized Solar Cells. *J. Phys. Chem. Lett.* **2,** 1998–2003 (2011).
40. Hod, I. *et al.* Dye versus Quantum Dots in Sensitized Solar Cells: Participation of Quantum Dot Absorber in the Recombination Process. *J. Phys. Chem. Lett.* **2,** 3032–3035 (2011).
41. Mora-Seró, I. & Bisquert, J. Breakthroughs in the Development of Semiconductor-Sensitized Solar Cells. *J. Phys. Chem. Lett.* **1,** 3046–3052 (2010).
42. Radich, J. G., Dwyer, R. & Kamat, P. V. Cu 2 S Reduced Graphene Oxide Composite for High-Efficiency Quantum Dot Solar Cells. Overcoming the Redox Limitations of S 2 – /S n 2– at the Counter Electrode. *J. Phys. Chem. Lett.* **2,** 2453–2460 (2011).
43. Kubelka, P. New Contributions to the Optics of Intensely Light-Scattering Materials. Part I. *J. Opt. Soc. Am.* **38,** 448–457 (1948).
44. Borensztein, Y., Delannoy, L., Djedidi, A., Barrera, R. G. & Louis, C. Monitoring of the Plasmon Resonance of Gold Nanoparticles in Au / TiO 2 Catalyst under Oxidative and Reducing Atmospheres. *J. Phys. Chem. C* **114,** 9008–9021 (2010).
45. Smolensky, E. D., Neary, M. C., Zhou, Y., Berquo, T. S. & Pierre, V. C. Fe_3O_4@organic@Au: core-shell nanocomposites with high saturation magnetisation as magnetoplasmonic MRI contrast agents. *Chem. Commun. (Camb).* **47,** 2149–51 (2011).
46. Chakkaravarthy, C. The nickel / Iron battery. *J. Power Sources* **35,** 21–35 (1991).

47. Developments, P., Technology, C., Future, T. H. E. & Nickel, O. F. Introduction The. *J. Power Sources* **12,** 177–192 (1984).
48. Walter, M. G. *et al.* Solar water splitting cells. *Chem. Rev.* **110,** 6446–73 (2010).
49. Wang, H. *et al.* An ultrafast nickel-iron battery from strongly coupled inorganic nanoparticle/nanocarbon hybrid materials. *Nat. Commun.* **3,** 917 (2012).
50. Currao, A. Photoelectrochemical Water Splitting. *Chim. Int. J. Chem.* **61,** 815–819 (2007).